J. Appl. Comput. Mech., xx(x) (2026) 1-24
DOI: 10.22055/jacm.2026.49407.5954

ISSN: 2383-4536
jacm.scu.ac.ir

Shahid Chamran University of Ahvaz

Journal of Applied and Computational Mechanics

Research Paper

Simulation of Triple Stratified 3-D Bioconvective Non-Newtonian Nanofluid Flow using Physics-Informed Neural Network

Shweta Mishra

Department of Applied Mathematics, Maulana Abul Kalam Azad University of Technology, Haringhata, Nadia-741249, India, Email: shweta9935@gmail.com

Received May 25 2026; Revised August 29 2026; Accepted for publication August 31 2026.
✉ Corresponding author: S. Mishra (shweta9935@gmail.com)

Abstract. This study presents a Physics-Informed Neural Network (PINN) framework for the three-dimensional, bioconvective Carreau–Yasuda nanofluid flow over bi-directional stretching surfaces, incorporating Rosseland quadratic thermal radiation, Cattaneo–Christov heat and mass flux, dual-variable thermal conductivity and mass diffusivity with triple stratification. The governing partial differential equations are reduced using similarity transformation to a coupled, highly nonlinear ordinary differential equation system for velocity, temperature, concentration, and microorganism density, which the PINN solves directly by embedding the governing operators and boundary conditions in its loss function, without labeled training data. This work is framed as a quantitative feasibility and benchmarking study, evaluating where a mesh-free PINN currently stands relative to a Chebyshev spectral quasi-linearization method (SQLM) reference solution for this equation class. Pointwise comparison shows mean relative differences below 0.6% for the velocity, concentration, and microorganism density fields, with a higher deviation of 5.4% for temperature, engineering quantities agree with the SQLM reference within a maximum of 0.12% across the parameter combinations tested. Training diagnostics including boundary-condition residuals, PDE residuals, and loss convergence behavior are reported to characterize the numerical stability and current limitations of the PINN solution for this class of coupled bioconvective transport problems. The results indicate that while PINNs offer a mesh-free, gradient-based alternative capable of reproducing SQLM solutions to within engineering accuracy, SQLM retains a clear computational efficiency advantage for this boundary value problem.

Keywords: Carreau–Yasuda nanofluid, Rosseland quadratic thermal radiation, Thermal stratification, Solutal stratification, Microbial stratification, Cattaneo–Christov heat and mass flux.

1. Introduction

Physics-informed neural networks (PINNs) introduced by Raissi et al. [1] have transformed computational modelling in fluid mechanics, heat, and mass transfer by combining the collective approximation capabilities of neural networks with the implementation of governing physical laws, particularly partial differential equations (PDEs), into the loss function. PINNs provide a higher-performance and generalized neural network framework that observes the data patterns, incorporating physical laws. Zhang et al. [2] discussed the capabilities of PINNs in addressing the challenges in the modelling of complex fluid dynamics, while the re-initialization strategy for the stiff problem using PINNs was reported by Smith et al. [3]. The PINN model for fluid mechanics and engineering applications was reported by Patel et al. [4], while PINNs for learning undefined physics for non-Newtonian fluids were studied by Reyes et al. [5]. PINNs provide significant advantages by integrating governing equations directly into the loss function, enabling mesh-free solutions that can easily handle high-dimensional problems without any complex meshing requirements of traditional numerical methods. PINNs provide a meshless framework for solving forward and inverse problems in science and engineering, while other existing numerical and analytical techniques, such as finite element [6], finite volume [7], and spectral methods, such as single-variable [8, 9] and bivariate methods [10, 11], rely on grid discretization and often face difficulties in modelling complex multiphysics systems,

Computational fluid dynamics and artificial neural networks have transformed the solution capabilities for complex transport phenomena in complex fluid systems. Artificial Neural Networks (ANNs) have emerged as powerful computational tools for predicting and modelling complex heat and mass transfer. Jebali et al. [12] reported the importance of ANN in the prediction of entropy optimization, heat, and mass transfer in different engineering applications. Some recent investigations of ANN in computational fluid dynamics reflect higher accuracy and prediction capabilities. Ali et al. [13] utilized ANN for predicting the thermophysical properties of nanofluid heat transfer accurately, with lower mean squared error values and higher convergence rates. While Sahu et al. [14] integrated the Levenberg-Marquardt backpropagation algorithms to design hybrid neural network architectures that enable efficient training on complex datasets while maintaining high predictive accuracy, and the engine oil-based hybrid nanofluid model with ANN was discussed by Mishra et al. [15], which reflects better prediction of the heat transfer

Published online: September 03 2026

rate in an engine oil-based hybrid nanofluid. Moreover, hybrid models that integrate PINN or neuro-heuristic algorithms with regression methods have also been proposed as a means of enhancing the accuracy of predictions in the case of nanofluid flow through the inclusion of such systems into magnetohydrodynamic stratified flows [16], as well as into three-dimensional micropolar nanofluid flow systems with uncertainty quantification [17]. The adoption of PINNs in fluid mechanics has enabled accurate simulation of laminar and turbulent flow, multiphase dynamics, and non-Newtonian behaviors directly from data while remaining consistent with the underlying physics [3-5]. PINNs can provide a better solution even with a noisy or sparse numerical or experimental dataset, and a PINN model can also be designed by incorporating the Navier-Stokes equations and related boundary conditions into the training loss [18]. It also provides an accurate solution for the limited datasets (experimental/numerical) or data-free PINN framework through its physics-based loss function. It minimizes the importance of big data in the accurate prediction of heat and mass transfer in computational fluid mechanics.

The latest studies, including PINNs, have shown excellent alignment between surrogate modelling as well as directly simulating models in fluid mechanics problems. Kananipour et al. [19] studied heat and mass transfer by including the energy and species concentration equations in the nanofluid flowing in microchannels. This framework shows the accurate prediction of heat and mass transfer in porous medium, using the homotopy perturbation method. Different studies reported the capabilities of the PINNs framework in capturing coupled phenomena, such as thermophoresis, cross-diffusion, Brownian motion, and mixing of nanoparticles in the modelling of complex systems of flow, even including the energy, concentration, and microbial concentration phenomena.

The Carreau-Yasuda fluid model is essential for understanding the shear-thinning and shear-thickening characteristics of non-Newtonian fluids. Different studies involving these phenomena, such as the analysis of blood flow were studied by Qayyum et al. [20], while the bio-convection phenomena with magnetized properties were discussed by Waqas et al. [21], and the influence of quadratic thermal radiation was discussed by Chen et al. [22]. The properties of the non-Newtonian model are influenced by different parameters on various geometries, such as for peristaltic flow with ANN [23], while neuro-fuzzy simulation on an inclined plate was discussed by Salam et al. [24]. Not only do boundary layer flows alone require non-Newtonian nanofluid analysis, but their application to renewable energy systems has proven equally fruitful for this research field. For instance, the thermal efficiency and entropy generation of the Sisko nanofluids carrying carbon-based nanoparticles (graphene, graphene oxide, SWCNT) were studied by Raafat et al. [25] in the context of a parabolic trough solar collector, with the Sisko rheological parameters and nanoparticles influencing the results on skin friction and heat transfer.

Stratification is an important phenomenon in biological, geophysical, and engineering systems. The triple-stratification on a Riga plate incorporating microorganisms was discussed by Kumar et al. [26], while the stratification for bio-convective nanofluids with different parameters was discussed in [27, 28].

The bioconvective nanofluid is the phenomenon of mixing motile microorganisms into the nanofluid to study the characteristics of density variation. Bhatti et al. [29] discussed the oxytactic microorganisms incorporated into the water-based nanofluid. The microorganisms that are flowing against the gravitational force are known as gyrotactic microorganisms and are heavier than the water. This creates a dense upper layer of the fluid, causing unstable density stratification in the fluid, leading to hydromagnetic instability and unstable convection motion in the fluid. The presence of microorganisms and nanoparticles in the base fluid enhances the thermal properties, heat and mass transfer on different geometries, and is useful in different microfluidic devices [30, 31]. The impact of bioconvection on heat and mass transfer using a neural network for a two-phase magneto-Williamson nanofluid was discussed by Ali et al. [32].

Thermal conductivity is an important aspect of complex fluids for managing the heat transfer rate in different engineering applications, such as microelectronic devices, high-powered lasers, heat flux devices, including X-rays, and more. The dual variable of conductivity, including thermal and solutal conductivity in a Carreau-Yasuda nanofluid, was discussed by Waqas et al. [33]. The impact of variable thermal conductivity with Catteneo-Christov double diffusion was discussed by Khan et al. [34] to understand the heat and mass transfer phenomena in a three-dimensional non-Newtonian casson fluid, while stagnation point flow for a Maxwell nanofluid was discussed by [35], and Maxwell hybrid nanofluid was discussed by [36]. These effects are crucial and highly influenced by some other parameters, such as magnetic fields, chemical reactions, and microorganisms, where they interplay between the variable properties and external forces, creating highly nonlinear coupling.

Quadratic thermal radiation effects have become increasingly important in high-temperature applications where the traditional Rosseland approximation requires modification [37]. The quadratic form of thermal radiation, utilizing T^4 expansion and quadratic approximations for large temperature differences, provides more accurate predictions compared to linear radiation models [38]. Studies on quadratic thermal radiation show its influence on heat transfer and affect the boundary layer thickness [39], while the PINNs framework for the fluids, mainly focused on heat transfer, was discussed by Li et al. [40].

The Carreau-Yasuda flow with other critical mechanisms, such as triple stratification for heat transfer, using a hybrid model was discussed by Rana et al. [41], and using PINNs for the heat transfer channel was studied by Lee et al. [42]. These investigations reflected the efficiency of PINNs in capturing the transport mechanisms, stratification complexities, and energy efficiencies, which are useful in biomedical and industrial processes. The mesh-free nature and scalability of PINNs provide a high-fidelity and large-scale simulation for numerically complex problems. These data-free, inverse design, optimization, and uncertainty quantification help in achieving the required target for complex and numerically complicated problems, including energy, momentum, species, and microbial concentration equations that are used in different fields. However, PINNs reflect some limitations while applying on the complex systems, such as the architecture of the neural network, selection of hyperparameters, and learning rates. The limitations of PINNs for stiff problems were discussed by Lee et al. [43], while the prediction of 3-dimensional fluid flow with PINNS and the learning capabilities of PINNs were discussed by Heger et al. [44], and the limitations of PINNs were discussed by Huang [45]. These challenges highlighted the need for careful implementation, training process, and integration with the CFD or numerical method for generating the labelled data. There are some recent articles discussed and developed the intelligent systems using ANN and PINN on various application-based models [46, 47] using various fluid model and geometries. These studies provide an approach and their impact on the real-world applications and our investigation.

The primary objective of this work is to conduct a systematic computational assessment of a Physics-Informed Neural Network (PINN) framework for the bioconvective Carreau–Yasuda nanofluid model with triple stratification and quadratic thermal radiation. The performance of the PINN approach is benchmarked against the Spectral Quasi-Linearization Method (SQLM), which serves as a high-accuracy reference solution. The study emphasizes determining the accuracy of the PINN findings in predicting the results of bioconvective flows for all representative parameter ranges, including skin friction coefficients, Nusselt number, Sherwood number, and the rate at which microorganisms are transferred.

Based on the above literature, the present study, building on [48–51], develops a Physics-Informed Neural Network formulation for a three-dimensional Carreau–Yasuda nanofluid flow that simultaneously incorporates quadratic Rosseland thermal radiation and dual, temperature- and concentration-dependent variable conductivity within a bioconvective, triply stratified boundary layer. To the best of our knowledge, this specific combination of mechanisms has not previously been solved with a PINN. Rather than positioning the PINN as a replacement for existing spectral solvers, which, for this similarity-reduced ODE system, already achieve high accuracy at lower computational cost than the present training procedure, this work is framed as a quantitative feasibility and benchmarking study. It establishes, through pointwise profile comparison and engineering-quantity agreement against a Chebyshev spectral quasi-linearization (SQLM) reference solution, how accurately a standard, data-free PINN can track a high-fidelity solution for this class of strongly coupled, five-equation non-Newtonian bioconvective system, and where the current formulation's accuracy and computational trade-offs stand relative to SQLM. The purpose of this comparison is to provide motivation for future work on extending PINNs with parameters, such as inverse and parameter estimation problems, as well as meshless methods for data assimilation from noisy or sparse data, instead of claiming that a true advantage has already been shown.

2. Mathematical Model

This is a comprehensive study for a three-dimensional bioconvective Carreau–Yasuda nanofluid over bi-directional stretching surfaces with Rosseland quadratic thermal radiation, viscous dissipation, and chemical reaction, with temperature-dependent dual conductivity, while considering triple stratifications in the boundary layer.

The combination of mechanisms considered here is motivated by solar-assisted microbial bioreactor and biofuel-cell type systems, in which a nanoparticle-doped, gyrotactic-microorganism-laden suspension is processed under concentrated thermal/solar radiation for enhanced photobioreactor efficiency. In such systems, the carrier suspension is frequently shear-thinning or shear-thickening rather than Newtonian, motivating the Carreau–Yasuda rheology, an externally applied magnetic field is commonly used to control flow circulation and limit microorganism sedimentation, motivating the MHD terms, inlet feed streams typically enter at a different temperature, nanoparticle concentration, and microbial density than the ambient reactor fluid, motivating the triple stratification, and the wide operating-temperature range associated with solar/radiative heating makes a constant-conductivity assumption inaccurate, motivating the dual variable-conductivity treatment.

The remaining mechanisms, such as Brownian motion, thermophoresis, viscous dissipation, and chemical reaction, are the standard closure terms required once a nanofluid and a chemically active species coexist. The present formulation is therefore intended as a physically consistent, if idealized, model of such a coupled radiative–bioconvective–nanofluid system, rather than an arbitrary superposition of independently studied effects. The graphical representation of the model is shown in Fig. 1.

The stress tensor of the non-Newtonian Carreau-Yasuda nanofluid is defined as [20-22] to consider the shear-thinning and thickening properties by using five material parameters:

$$\breve{\tau} = \left[\mu_\infty + (\mu_0 - \mu_\infty)\left\{1 + (\Gamma\dot{\Upsilon})^d\right\}^{\frac{n-1}{d}}\right]\dot{A}_1 \tag{1}$$

Here, n is the power law parameter, d is the Carreau-Yasuda parameter, and the material rate constant is Γ. The shear rate of viscosity at ambient is μ_∞, while the zero shear rate of viscosity is μ_0. The shear strain is defined as:

$$\dot{\Upsilon} = \sqrt{\left(\frac{\partial u}{\partial z}\right)^2 + \left(\frac{\partial v}{\partial z}\right)^2} \tag{2}$$

and the Rivlin-Erickson tensor is defined as $\dot{A}_1 = [\nabla.\mathrm{V} + \nabla.\mathrm{V}^T]$. By assuming $\mu_\infty = 0$, Eq. (1) can be written as [45]:

$$\breve{\tau} = \left[\mu_0\left\{1 + (\Gamma\dot{\Upsilon})^d\right\}^{\frac{n-1}{d}}\right]\dot{A}_1 \tag{3}$$

The approximation of $\mu_\infty = 0$ [45] is justified in the case where the viscosity at the infinite shear rate is much smaller compared to the viscosity at the zero shear rate $(\mu_\infty \ll \mu_0)$, which is generally the assumption for the mathematical formulation that reduces the involved parameters, and is used in the Carreau-Yasuda boundary layer formulations. As the shear rate is maximum at the wall and tends to zero at infinity, the simplification makes a greater relative contribution at locations close to the wall where the skin friction is computed and is recognized to be such here.

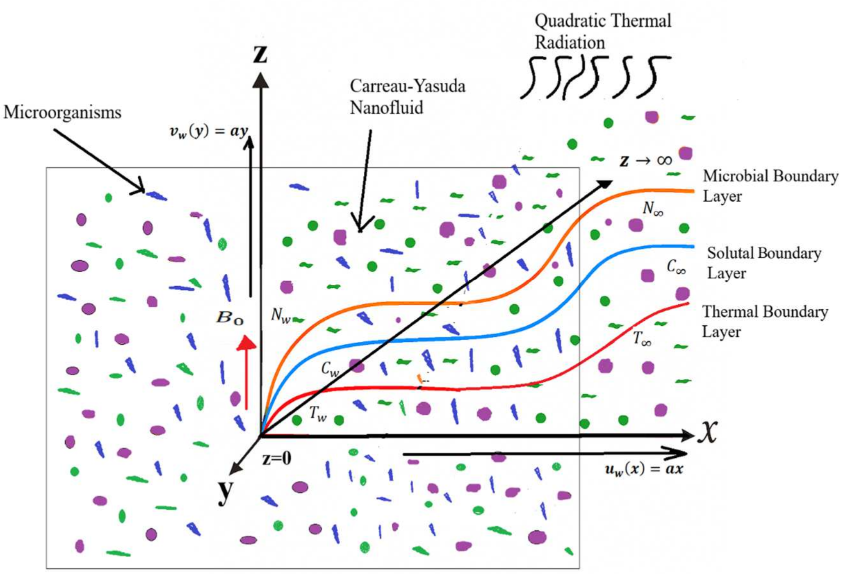

Fig. 1. Graphical representation of the bioconvective Carreau-Yasuda Model.

The nanofluid is treated as a homogeneous generalized non-Newtonian fluid following the Carreau–Yasuda rheological model. A uniform magnetic field acts in the transverse direction (z-axis), while the induced magnetic field is neglected under the standard low-magnetic-Reynolds-number assumption, $Re_m = \mu_0 \sigma U L \ll 1$, which holds for the weakly conducting nanofluid systems and characteristic velocities and length scales considered here. The electrical conductivity σ is treated as a constant material property in the present model, independent of the local, shear-rate-dependent apparent viscosity of the Carreau–Yasuda fluid. A fully coupled electro-rheological formulation in which σ itself varies with shear rate is not considered here and is noted as a simplification of the present model. The formulation also accounts for viscous dissipation and quadratic Rosseland radiation effects. The influence of Brownian motion, motile microorganisms, and thermophoresis is also integrated. The triple stratifications at boundary layers are used to calculate the mass, energy, and microbial density transfer in the model [49, 50]. The flow is steady, incompressible, three-dimensional over stretching planes with velocities $u_w(x) = ax$ and $v_w(y) = ay$, in an applied transverse magnetic field B_0. The Carreau–Yasuda constitutive law enters via an effective viscosity operator in the normal shear directions. With buoyancy due to temperature T, nanoparticle concentration C, and microorganism density N, the model [48-51]:

$$\frac{\partial u}{\partial x} + \frac{\partial v}{\partial y} + \frac{\partial w}{\partial z} = 0 \tag{4}$$

$$\begin{aligned}
&\frac{\partial u}{\partial x} + v\frac{\partial u}{\partial y} + w\frac{\partial u}{\partial z} = u_\infty \frac{du_\infty}{dx} + \nu \frac{\partial^2 u}{\partial z^2}\left[1 + \left(\frac{n-1}{d}\right)(d+2)\Gamma^d \left\{\left(\frac{\partial u}{\partial z}\right)^2 + \left(\frac{\partial v}{\partial z}\right)^2\right\}^{\left(\frac{d}{2}\right)}\right]^{\left(\frac{n-1}{d}\right)} \\
&\times\left[1 + \left(\frac{n-1}{d}\right)(d+2)\Gamma^d \left\{\left(\frac{\partial u}{\partial z}\right)^2 + \left(\frac{\partial v}{\partial z}\right)^2\right\}^{\left(\frac{d-2}{2}\right)}\left[1 + \left(\frac{n-1}{d}\right)(d+2)\Gamma^d \left\{\left(\frac{\partial u}{\partial z}\right)^2 + \left(\frac{\partial v}{\partial z}\right)^2\right\}^{\left(\frac{d}{2}\right)}\right]^{-1}\left(\frac{\partial u}{\partial z}\right)^2\right] \\
&+\left[\left(\frac{n-1}{d}\right)(d+2)\Gamma^d \left\{\left(\frac{\partial u}{\partial z}\right)^2 + \left(\frac{\partial v}{\partial z}\right)^2\right\}^{\left(\frac{d-2}{2}\right)}\left[1 + \left(\frac{n-1}{d}\right)(d+2)\Gamma^d \left\{\left(\frac{\partial u}{\partial z}\right)^2 + \left(\frac{\partial v}{\partial z}\right)^2\right\}^{\left(\frac{d}{2}\right)}\right]^{-1}\frac{\partial u}{\partial z}\frac{\partial v}{\partial z}\frac{\partial^2 v}{\partial z^2}\right] - \frac{\sigma B_0^2}{\rho_f}(u - u_\infty) \\
&+\frac{\mathrm{g_t}\ \beta}{\rho_\mathrm{f}}(1 - \mathrm{C}_\infty)\ (\mathrm{T} - \mathrm{T}_\infty) + \frac{\mathrm{g_t}}{\rho_\mathrm{f}}\left(\rho_\mathrm{p} - \rho_\mathrm{f}\right)(\mathrm{C} - \mathrm{C}_\infty) + \frac{\gamma\ \mathrm{g_t}}{\rho_\mathrm{f}}(\rho_\mathrm{m} - \rho_\mathrm{f})(\mathrm{N} - \mathrm{N}_\infty).
\end{aligned} \tag{5}$$

$$\begin{aligned}
&u\frac{\partial v}{\partial x} + v\frac{\partial v}{\partial y} + w\frac{\partial v}{\partial z} = \nu \frac{\partial^2 v}{\partial z^2}\left[1 + \left(\frac{n-1}{d}\right)(d+2)\Gamma^d \left\{\left(\frac{\partial u}{\partial z}\right)^2 + \left(\frac{\partial v}{\partial z}\right)^2\right\}^{\left(\frac{d}{2}\right)}\right]^{\left(\frac{n-1}{d}\right)} \\
&\times\left[1 + \left(\frac{n-1}{d}\right)(d+2)\Gamma^d \left\{\left(\frac{\partial u}{\partial z}\right)^2 + \left(\frac{\partial v}{\partial z}\right)^2\right\}^{\left(\frac{d-2}{2}\right)}\left[1 + \left(\frac{n-1}{d}\right)(d+2)\Gamma^d \left\{\left(\frac{\partial u}{\partial z}\right)^2 + \left(\frac{\partial v}{\partial z}\right)^2\right\}^{\left(\frac{d}{2}\right)}\right]^{-1}\left(\frac{\partial v}{\partial z}\right)^2\right] \\
&+\left[1 + \left(\frac{n-1}{d}\right)(d+2)\Gamma^d \left\{\left(\frac{\partial u}{\partial z}\right)^2 + \left(\frac{\partial v}{\partial z}\right)^2\right\}^{\left(\frac{d-2}{2}\right)}\left[1 + \left(\frac{n-1}{d}\right)(d+2)\Gamma^d \left\{\left(\frac{\partial u}{\partial z}\right)^2 + \left(\frac{\partial v}{\partial z}\right)^2\right\}^{\left(\frac{d}{2}\right)}\right]^{-1}\frac{\partial u}{\partial z}\frac{\partial v}{\partial z}\frac{\partial^2 u}{\partial z^2}\right] - \frac{\sigma B_0^2}{\rho_f}v.
\end{aligned} \tag{6}$$

$$\begin{aligned}
&u\frac{\partial T}{\partial x} + v\frac{\partial T}{\partial y} + w\frac{\partial T}{\partial z} + \Lambda_T\left[u^2\frac{\partial^2 T}{\partial x^2} + v^2\frac{\partial^2 T}{\partial y^2} + w^2\frac{\partial^2 T}{\partial z^2} + 2uv\frac{\partial^2 T}{\partial x \partial y} + 2vw\frac{\partial^2 T}{\partial y \partial z} + 2uw\frac{\partial^2 T}{\partial x \partial z} + u\frac{\partial u}{\partial x}\frac{\partial T}{\partial x} + v\frac{\partial u}{\partial y}\frac{\partial T}{\partial x} + w\frac{\partial u}{\partial z}\frac{\partial T}{\partial x} + u\frac{\partial v}{\partial x}\frac{\partial T}{\partial y}\right. \\
&\qquad\left. + v\frac{\partial v}{\partial y}\frac{\partial T}{\partial y} + w\frac{\partial v}{\partial z}\frac{\partial T}{\partial y} + u\frac{\partial w}{\partial x}\frac{\partial T}{\partial z} + v\frac{\partial w}{\partial y}\frac{\partial T}{\partial z} + w\frac{\partial w}{\partial z}\frac{\partial T}{\partial z}\right] \\
&\qquad= \frac{1}{\rho c_p}\frac{\partial}{\partial z}\left[K(T)\frac{\partial T}{\partial z}\right] + \tau\left[D_B\frac{\partial T}{\partial z}\frac{\partial C}{\partial z} + \frac{D_T}{T_\infty}\left(\frac{\partial T}{\partial z}\right)^2 + D_N\frac{\partial T}{\partial z}\frac{\partial N}{\partial z}\right] - \frac{1}{\rho c_p}\frac{\partial}{\partial z}\left(\frac{4\sigma^*}{3\mathrm{k}^*}\frac{\partial T^4}{\partial z}\right) \\
&\qquad+ \frac{\mu_0}{\rho c_p}\left\{\left(\frac{\partial u}{\partial z}\right)^2 + \left(\frac{\partial v}{\partial z}\right)^2\right\}\left[1 + \left(\frac{n-1}{d}\right)(d+2)\Gamma^d\left\{\left(\frac{\partial u}{\partial z}\right)^2 + \left(\frac{\partial v}{\partial z}\right)^2\right\}^{d/2}\right]^{\left(\frac{n-1}{d}\right)} + \frac{\sigma B_0^2}{\rho_f}(u^2 + v^2).
\end{aligned} \tag{7}$$

$$\begin{aligned}
&u\frac{\partial C}{\partial x} + v\frac{\partial C}{\partial y} + w\frac{\partial C}{\partial z} + \Lambda_C\left[u^2\frac{\partial^2 C}{\partial x^2} + v^2\frac{\partial^2 C}{\partial y^2} + w^2\frac{\partial^2 C}{\partial z^2} + 2uv\frac{\partial^2 C}{\partial x \partial y} + 2vw\frac{\partial^2 C}{\partial y \partial z} + 2uw\frac{\partial^2 C}{\partial x \partial z} + u\frac{\partial u}{\partial x}\frac{\partial C}{\partial x} + v\frac{\partial u}{\partial y}\frac{\partial C}{\partial x} + w\frac{\partial u}{\partial z}\frac{\partial C}{\partial x} + u\frac{\partial v}{\partial x}\frac{\partial C}{\partial y}\right. \\
&\qquad\left. + v\frac{\partial v}{\partial y}\frac{\partial C}{\partial y} + w\frac{\partial v}{\partial z}\frac{\partial C}{\partial y} + u\frac{\partial w}{\partial x}\frac{\partial C}{\partial z} + v\frac{\partial w}{\partial y}\frac{\partial C}{\partial z} + w\frac{\partial w}{\partial z}\frac{\partial C}{\partial z}\right] = \frac{1}{\rho c_p}\frac{\partial}{\partial z}\left[D(T)\frac{\partial C}{\partial z}\right] + \mathrm{D_B}\frac{\partial^2 \mathrm{C}}{\partial \mathrm{z}^2} + \frac{D_T}{T_\infty}\frac{\partial^2 T}{\partial y^2} - k_c(\mathrm{C} - \mathrm{C}_\infty).
\end{aligned} \tag{8}$$

$$u\frac{\partial N}{\partial x} + v\frac{\partial N}{\partial y} + w\frac{\partial N}{\partial z} + \frac{\mathrm{mW_c}}{\Delta \mathrm{C}}\left[\frac{\partial N}{\partial z}\frac{\partial \mathrm{C}}{\partial \mathrm{Z}} + N\frac{\partial^2 \mathrm{C}}{\partial \mathrm{z}^2}\right] = \mathrm{D}_N\frac{\partial^2 \mathrm{N}}{\partial \mathrm{z}^2} + \frac{D_T}{T_\infty}\frac{\partial^2 T}{\partial z^2} \tag{9}$$

This momentum equation consists of the nonlinear Carreau–Yasuda diffusion, MHD drag, and mixed convection due to T, C, and N gradients. The x-momentum includes free-stream acceleration, buoyancy terms, and magnetic damping, while the y-momentum includes analogous Carreau–Yasuda diffusion and magnetic influence. Here u, v, and w are the velocity profiles in x, y, and z directions, while the velocity for the free stream is u_∞. The density of the fluid is denoted as ρ_f, the heat capacity of the fluid ρc_f, the kinematic viscosity is ν, $\mathrm{g_t}$ is the gravitational force, the expansion of volumetric coefficient by β, the nanoparticles density is ρ_p, and microbial density is ρ_m, the microbial average volume by γ, and the electrical conductivity by σ.

The energy equation consists of convection–diffusion with temperature-dependent conductivity $K(T) = k_\infty\left\{1 + \omega_1\ \frac{T - T_\infty}{T_w - T_0}\right\}$ [33], quadratic Rosseland radiation via T^4 expansion, viscous dissipation under Carreau–Yasuda rheology, Joule heating, and C–T–N cross-diffusive couplings (D_B, D_T, D_N). The non-Fourier heat flux relaxation Λ_T is introduced through the Cattaneo–Christov formulation as a thermal relaxation time coefficient; although the base flow is steady, the relaxation term modifies the constitutive flux–gradient relationship itself rather than only the transient response, consistent with its established use in steady Carreau-type bioconvective flows [34]. The quadratic radiation uses a Taylor expansion. Here, the temperature at the wall is denoted by T_w, while T_∞ is the temperature at ambient. The thermal conductivity at ambient is k_∞, while ω_1 is the minor scalar variable used to calculate the temperature power using thermal conductivity, the ratio of heat capacity of the nanoparticle to the base fluid by τ. The Brownian, thermophoresis diffusion, and microbial thermophoresis diffusion coefficients by D_B, D_T, and $D_{N,}$ respectively, while radiative heat flux by q_r, σ^* is the Stefan-Boltzmann constant, and k^* is the mean absorption coefficient.

The species concentration equation consists of convection–diffusion with variable solutal conductivity $D(T) = D_\infty \left\{1 + \omega_2 \, \frac{C - C_\infty}{C_w - C_0}\right\}$ [33], Brownian and thermophoretic effects, chemical reaction, and the solutal analogue of the Cattaneo–Christov relaxation, with Λ_C the solutal relaxation time parameter. Even though there exists no macroscopic time dependence, Cattaneo–Christov theory changes the definition of the constitutive equation of the heat/mass flux in terms of its corresponding gradient. Thus, it is possible for the relaxation coefficients Λ_T and Λ_C to be nonzero even in a steady formulation of the boundary layer. Here, the concentration of the fluid at the wall is defined by C_w , while C_∞ is the concentration at ambient. The mass conductivity at ambient is D_∞, k_c is the chemical reaction constant, while ω_2 is the minor scalar variable used to calculate the concentration using solutal conductivity.

The microbial concentration equation consists of convection–diffusion with chemotaxis coupling to concentration, and thermal cross-diffusion. The chemotaxis term arises from a directed swimming (chemotactic) flux of motile microorganisms along the gradient of the nanoparticle concentration field, following the standard bioconvection closure in which microorganisms respond to a chemical stimulus gradient (an extension, adopted from the bioconvection-nanofluid literature, of the classical oxytactic bioconvection framework in which the stimulus is conventionally a dissolved nutrient or oxygen field rather than nanoparticle concentration). This produces a gradient–gradient correlation term between the microorganism and concentration profiles, and a term representing bulk advection of the local microorganism population by the curvature of the concentration field. The thermal cross-diffusion term represents a thermophoretic-type drift of motile microorganisms along the temperature gradient, analogous to the thermophoretic transport already included for the nanoparticles; this is captured through the microbial thermophoresis diffusion coefficient D_N, which plays the same physical role for the microorganism field that D_T plays for the nanoparticle concentration field. Here, microbial concentration of the fluid at the wall is defined by N_w, while N_∞ is the microbial concentration at the ambient. The microbial thermophoresis diffusion is D_{N}, W_c is the maximum cell swimming speed, and the chemotaxis constant is denoted by m. For the modelling, mW_c is considered to be constant.

The thermal radiation in Equ. (7) is calculated by employing the Roseland approximation [37-39]:

$$q_r = -\frac{4\sigma^*}{3\mathrm{k}^*}\frac{\partial T^4}{\partial y} \tag{10}$$

The expansion through Taylor's series is exploited to develop the T^4 term as:

$$T^4 \cong T_\infty^4 + 4(\mathrm{T} - T_\infty)T_\infty^3 + 6(\mathrm{T} - T_\infty)^2 T_\infty^2 + \cdots \tag{11}$$

For adequately large temperature deviations, the quadratic approximation should be utilized since the term would substantially impact the heat transfer. Thus, we have:

$$T^4 \cong 3T_\infty^4 + 6T_\infty^2 T^2 - 8T_\infty^3 T \tag{12}$$

The boundary conditions [21, 25, 26, 48, 50] for the considered model are given as:

$$\begin{aligned} &u = u_w(x) = ax, \quad v = v_w(y) = ay, \quad w = 0, \quad T = T_w = T_0 + c_1 x, \quad C = C_w = C_0 + d_1 x, \quad N = N_w = N_0 + e_1 x, at \;\; z = 0, \\ &u = u_\infty(x) = bx, \quad T \to T_\infty = T_0 + c_2 x, \quad C \to C_\infty = C_0 + d_2 x, \quad N \to N_\infty = N_0 + e_2 x, \quad as \; z \to \infty, \end{aligned} \tag{13}$$

Here a and b are dimensionless constants, while for the stratification in the Carreau-Yasuda nanofluid model, the thermal stratification is defined at the wall and ambient, similarly for the solutal and microbial stratifications with respect to the corresponding reference temperature, species, and microbial concentrations, i.e., T_0, C_0, N_0. Here, the temperature coefficients associated with temperature stratification are c_1 and c_2, while d_1 and d_2 are the nanoparticle concentration coefficients for solutal, with e_1 and e_2 as microbial concentration coefficients for the microbial stratifications.

The residual of the governing PDEs from Eqs. (5-9) can be written as:

$$\begin{aligned} F = {} & u\frac{\partial u}{\partial x} + v\frac{\partial u}{\partial y} + w\frac{\partial u}{\partial z} - u_\infty\frac{du_\infty}{dx} - \nu\frac{\partial^2 u}{\partial z^2}\left[1 + \left(\frac{n-1}{d}\right)(d+2)\Gamma^d\left\{\left(\frac{\partial u}{\partial z}\right)^2 + \left(\frac{\partial v}{\partial z}\right)^2\right\}^{\left(\frac{d}{2}\right)}\right]^{\left(\frac{n-1}{d}\right)} \\ & \times\left[1 + \left(\frac{n-1}{d}\right)(d+2)\Gamma^d\left\{\left(\frac{\partial u}{\partial z}\right)^2 + \left(\frac{\partial v}{\partial z}\right)^2\right\}^{\left(\frac{d-2}{2}\right)}\left[1 + \left(\frac{n-1}{d}\right)(d+2)\Gamma^d\left\{\left(\frac{\partial u}{\partial z}\right)^2 + \left(\frac{\partial v}{\partial z}\right)^2\right\}^{\left(\frac{d}{2}\right)}\right]^{-1}\left(\frac{\partial u}{\partial z}\right)^2\right] \\ & -\left[\left(\frac{n-1}{d}\right)(d+2)\Gamma^d\left\{\left(\frac{\partial u}{\partial z}\right)^2 + \left(\frac{\partial v}{\partial z}\right)^2\right\}^{\left(\frac{d-2}{2}\right)}\left[1 + \left(\frac{n-1}{d}\right)(d+2)\Gamma^d\left\{\left(\frac{\partial u}{\partial z}\right)^2 + \left(\frac{\partial v}{\partial z}\right)^2\right\}^{\left(\frac{d}{2}\right)}\right]^{-1}\frac{\partial u}{\partial z}\frac{\partial v}{\partial z}\frac{\partial^2 v}{\partial z^2}\right] + \frac{\sigma B_0^2}{\rho_f}(u - u_\infty) \\ & -\frac{\mathrm{g_t}\;\beta}{\rho_\mathrm{f}}(1 - \mathrm{C}_\infty)\,(\mathrm{T} - \mathrm{T}_\infty) + \frac{\mathrm{g_t}}{\rho_\mathrm{f}}\,\left(\rho_\mathrm{p} - \rho_\mathrm{f}\right)(\mathrm{C} - \mathrm{C}_\infty) + \frac{\gamma\;\mathrm{g_t}}{\rho_\mathrm{f}}(\rho_\mathrm{m} - \rho_\mathrm{f})(\mathrm{N} - \mathrm{N}_\infty) \end{aligned} \tag{14}$$

$$\begin{aligned} G = {} & u\frac{\partial v}{\partial x} + v\frac{\partial v}{\partial y} + w\frac{\partial v}{\partial z} - \nu\frac{\partial^2 v}{\partial z^2}\left[1 + \left(\frac{n-1}{d}\right)(d+2)\Gamma^d\left\{\left(\frac{\partial u}{\partial z}\right)^2 + \left(\frac{\partial v}{\partial z}\right)^2\right\}^{\left(\frac{d}{2}\right)}\right]^{\left(\frac{n-1}{d}\right)} \\ & \times\left[1 + \left(\frac{n-1}{d}\right)(d+2)\Gamma^d\left\{\left(\frac{\partial u}{\partial z}\right)^2 + \left(\frac{\partial v}{\partial z}\right)^2\right\}^{\left(\frac{d-2}{2}\right)}\left[1 + \left(\frac{n-1}{d}\right)(d+2)\Gamma^d\left\{\left(\frac{\partial u}{\partial z}\right)^2 + \left(\frac{\partial v}{\partial z}\right)^2\right\}^{\left(\frac{d}{2}\right)}\right]^{-1}\left(\frac{\partial v}{\partial z}\right)^2\right] \\ & -\left[1 + \left(\frac{n-1}{d}\right)(d+2)\Gamma^d\left\{\left(\frac{\partial u}{\partial z}\right)^2 + \left(\frac{\partial v}{\partial z}\right)^2\right\}^{\left(\frac{d-2}{2}\right)}\left[1 + \left(\frac{n-1}{d}\right)(d+2)\Gamma^d\left\{\left(\frac{\partial u}{\partial z}\right)^2 + \left(\frac{\partial v}{\partial z}\right)^2\right\}^{\left(\frac{d}{2}\right)}\right]^{-1}\frac{\partial u}{\partial z}\frac{\partial v}{\partial z}\frac{\partial^2 u}{\partial z^2}\right] + \frac{\sigma B_0^2}{\rho_f}v, \end{aligned} \tag{15}$$

$$\begin{aligned}\Theta = {} & u\frac{\partial T}{\partial x}+v\frac{\partial T}{\partial y}+w\frac{\partial T}{\partial z} \\ & +\Lambda_T\left[u^2\frac{\partial^2 T}{\partial x^2}+v^2\frac{\partial^2 T}{\partial y^2}+w^2\frac{\partial^2 T}{\partial z^2}+2uv\frac{\partial^2 T}{\partial x\partial y}+2vw\frac{\partial^2 T}{\partial y\partial z}+2uw\frac{\partial^2 T}{\partial x\partial z}+u\frac{\partial u}{\partial x}\frac{\partial T}{\partial x}+v\frac{\partial u}{\partial y}\frac{\partial T}{\partial x}+w\frac{\partial u}{\partial z}\frac{\partial T}{\partial x}+u\frac{\partial v}{\partial x}\frac{\partial T}{\partial y}+v\frac{\partial v}{\partial y}\frac{\partial T}{\partial y}+w\frac{\partial v}{\partial z}\frac{\partial T}{\partial y}\right. \\ & \left.+u\frac{\partial w}{\partial x}\frac{\partial T}{\partial z}+v\frac{\partial w}{\partial y}\frac{\partial T}{\partial z}+w\frac{\partial w}{\partial z}\frac{\partial T}{\partial z}\right]-\frac{1}{\rho c_p}\frac{\partial}{\partial z}\left[K(T)\frac{\partial T}{\partial z}\right]-\tau\left[D_B\frac{\partial T}{\partial z}\frac{\partial C}{\partial z}+\frac{D_T}{T_\infty}\left(\frac{\partial T}{\partial z}\right)^2+D_N\frac{\partial T}{\partial z}\frac{\partial N}{\partial z}\right]+\frac{1}{\rho c_p}\frac{\partial}{\partial z}\left(\frac{4\sigma^*}{3\mathrm{k}^*}\frac{\partial T^4}{\partial z}\right) \\ & -\frac{\mu_0}{\rho c_p}\left\{\left(\frac{\partial u}{\partial z}\right)^2+\left(\frac{\partial v}{\partial z}\right)^2\right\}\left[1+\left(\frac{n-1}{d}\right)(d+2)\Gamma^d\left\{\left(\frac{\partial u}{\partial z}\right)^2+\left(\frac{\partial v}{\partial z}\right)^2\right\}^{d/2}\right]^{\left(\frac{n-1}{d}\right)}-\frac{\sigma B_0^2}{\rho_f}(u^2+v^2),\end{aligned} \tag{16}$$

$$\begin{aligned}\Phi = {} & u\frac{\partial C}{\partial x}+v\frac{\partial C}{\partial y}+w\frac{\partial C}{\partial z} \\ & +\Lambda_C\left[u^2\frac{\partial^2 C}{\partial x^2}+v^2\frac{\partial^2 C}{\partial y^2}+w^2\frac{\partial^2 C}{\partial z^2}+2uv\frac{\partial^2 C}{\partial x\partial y}+2vw\frac{\partial^2 C}{\partial y\partial z}+2uw\frac{\partial^2 C}{\partial x\partial z}+u\frac{\partial u}{\partial x}\frac{\partial C}{\partial x}+v\frac{\partial u}{\partial y}\frac{\partial C}{\partial x}+w\frac{\partial u}{\partial z}\frac{\partial C}{\partial x}+u\frac{\partial v}{\partial x}\frac{\partial C}{\partial y}+v\frac{\partial v}{\partial y}\frac{\partial C}{\partial y}\right. \\ & \left.+w\frac{\partial v}{\partial z}\frac{\partial C}{\partial y}+u\frac{\partial w}{\partial x}\frac{\partial C}{\partial z}+v\frac{\partial w}{\partial y}\frac{\partial C}{\partial z}+w\frac{\partial w}{\partial z}\frac{\partial C}{\partial z}\right]-\frac{1}{\rho c_p}\frac{\partial}{\partial z}\left[D(T)\frac{\partial C}{\partial z}\right]-\mathrm{D_B}\frac{\partial^2 \mathrm{C}}{\partial \mathrm{z}^2}+\frac{D_T}{T_\infty}\frac{\partial^2 T}{\partial y^2}+k_c(\mathrm{C}-\mathrm{C}_\infty),\end{aligned} \tag{17}$$

$$\mathrm{X} = u\frac{\partial N}{\partial x}+v\frac{\partial N}{\partial y}+w\frac{\partial N}{\partial z}+\frac{\mathrm{mW_c}}{\Delta \mathrm{C}}\left[\frac{\partial N}{\partial z}\frac{\partial \mathrm{C}}{\partial \mathrm{Z}}+N\frac{\partial^2 \mathrm{C}}{\partial \mathrm{z}^2}\right]-\mathrm{D}_N\frac{\partial^2 \mathrm{N}}{\partial \mathrm{z}^2}-\frac{D_T}{T_\infty}\frac{\partial^2 T}{\partial z^2}. \tag{18}$$

The following similarity transformations [48-51] are introduced to obtain the dimensionless form for the numerical technique:

$$\begin{gathered} u = axf'(\eta), \qquad v = ayg'(\eta), \qquad w = -\sqrt{av}[f(\eta)+g(\eta)], \qquad \eta = z\sqrt{\frac{a}{v}}\,, \\ T = T_\infty\{1+(\theta_w-1)\theta(\eta)\}, \quad T-T_\infty = (T_w-T_0)\theta(\eta), \\ C-C_\infty = (C_w-C_0)\varphi(\eta), N-N_\infty = (N_w-N_0)\xi(\eta). \end{gathered} \tag{19}$$

Here η is the dimensionless similarity variable. The above similarity transformation from Eq. (19) satisfies the continuity equation (Eq. (4)), and the other governing equations are transformed into the following non-linear coupled ordinary differential equations:

$$\begin{aligned} & f'''\left[1+\left(\frac{n-1}{d}\right)(d+2)\left({We_1}^2\ f''^2+{We_2}^2\ g''^2\right)^{\left(\frac{d}{2}\right)}\right]^{\left(\frac{n-1}{d}\right)} \\ & +\left[1+\left(\frac{n-1}{d}\right)(d+2)\left({We_1}^2\ f''^2+{We_2}^2\ g''^2\right)^{\left(\frac{d}{2}\right)}\right]^{\left(\frac{n-1}{d}\right)}\left\{\left(\frac{n-1}{d}\right)(d\right. \\ & \left.+2)\left({We_1}^2\ f''^2+{We_2}^2\ g''^2+\delta^2\right)^{\left(\frac{d-2}{2}\right)}f''^{[{We_1}^2 f'' f'''+{We_2}^2 g'' g''']}\right\}\left[1+\left(\frac{n-1}{d}\right)(d+2)\left({We_1}^2\ f''^2+{We_2}^2\ g''^2\right)^{\left(\frac{d}{2}\right)}\right]^{-1}-(f')^2 \\ & +f''(f+g)+A^2-M(f'-A)+\lambda(\theta-Nr\varphi-Rb\xi) = 0, \end{aligned} \tag{20}$$

$$\begin{aligned} & g'''\left[1+\left(\frac{n-1}{d}\right)(d+2)\left({We_1}^2\ f''^2+{We_2}^2\ g''^2\right)^{\left(\frac{d}{2}\right)}\right]^{\left(\frac{n-1}{d}\right)} \\ & +\left[1+\left(\frac{n-1}{d}\right)(d+2)\left({We_1}^2\ f''^2+{We_2}^2\ g''^2\right)^{\left(\frac{d}{2}\right)}\right]^{\left(\frac{n-1}{d}\right)}\left\{\left(\frac{n-1}{d}\right)(d\right. \\ & \left.+2)\left({We_1}^2\ f''^2+{We_2}^2\ g''^2+\delta^2\right)^{\left(\frac{d-2}{2}\right)}g''^{[{We_1}^2 f'' f'''+{We_2}^2 g'' g''']}\right\}\left[1+\left(\frac{n-1}{d}\right)(d+2)\left({We_1}^2\ f''^2+{We_2}^2\ g''^2\right)^{\left(\frac{d}{2}\right)}\right]^{-1}-(g')^2 \\ & +g''(f+g)-Mg' = 0, \end{aligned} \tag{21}$$

$$\begin{aligned} & \left[1+\omega_1\theta+4Rd(\theta_w-1)\theta+\frac{4}{3}Rd\right]\theta''+[\omega_1+4Rd(\theta_w-1)]\theta'^2-Pr(S_1+\theta)\,f'+Pr(f+g)\,\theta'-Pr\delta_T(f+g)^2\theta''+2Pr\delta_T(S_1+\theta)Lb_1(f+g)f'\theta' \\ & \quad -Pr\delta_T(S_1+\theta)(f')^2+Pr\delta_T(S_1+\theta)(f+g)f''-Pr\delta_T(f+g)(f'+g')\theta'+Pr\left[Nb\theta'\varphi'+Nt\theta'^2+Np\theta'\xi'\right] \\ & \quad +PrEcM\left(f'^2+g'^2\right)+PrEc\left[1+\left({We_1}^2\ f''^2+{We_2}^2\ g''^2\right)^{\left(\frac{d}{2}\right)}\right]^{\left(\frac{n-1}{d}\right)}\left(f''^2+g''^2\right)=0, \end{aligned} \tag{22}$$

$$\begin{gathered} \varphi''+Le(1+\omega_2\varphi)\varphi''+\omega_2 Le\varphi'^2+\left(\tfrac{Nt}{Nb}\right)\theta''-LePr(S_2+\varphi)\,f'+LePr(f+g)\varphi'-LePr\delta_C(f+g)^2\varphi''+2LePr\delta_C(S_2+\varphi)Lb_2(f+g)f'\varphi'-LePr \\ \delta_C(S_2+\varphi)(f')^2+LePr\delta_C(S_2+\varphi)(f+g)f''-LePr\delta_C(f+g)(f'+g')\varphi'-LePrCr\varphi=0, \end{gathered} \tag{23}$$

$$\xi''+Sb(f+g)\xi'-Sb(S_3+\xi)\,f'+\left(\frac{Nt}{Np}\right)\theta''-Pb[\xi'\varphi'+(\Omega+\xi)\varphi''+S_3\varphi'']=0. \tag{24}$$

along with the transformed boundary conditions:

$$\begin{gathered} f(0)=0, f'(0)=1, g(0)=0, g'(0)=1, \qquad \theta(0)=1-S_1,, \varphi(0)=1-S_2, \qquad \xi(0)=1-S_3, \quad at\ \ \eta=0, \\ f'(\infty)\to A, g'(\infty)\to 0, \theta(\infty)\to 0\ , \varphi(\infty)\to 0, \qquad , \xi(\infty)\to 0, \qquad at\ \ \eta\to\infty. \end{gathered} \tag{25}$$

Physically, the no-slip/no-penetration boundary conditions ensure that the fluid adjacent to the stretching surface follows the motion of the surface itself, in agreement with the physics of continuum flow near the solid-fluid interface. The wall properties T_w, C_w, N_w and their linear-in-x dependence represent the properties of a surface where the temperature, nanoparticle volume fraction and microorganism density vary systematically in the direction of stretching, assuming for continuous stretching-sheet processes like extrusion, continuous casting, or coating, which involve non-uniform surface properties.

The ambient conditions, on the other hand, represent a corresponding linear dependence in the free stream, corresponding to an existing stratification in the surrounding medium, as is seen in thermally or chemically stratified reservoirs, lakes or bioreactor inlet flows. The ratio of stratification coefficients between the ambient and the wall thus determines whether the wall-to-ambient gradient responsible for heat, mass and microorganism transfer is increased or reduced compared to the unstratified case, and this ratio is the physical basis for the triple stratification effects analyzed in the Results section.

The parameters are the local Weissenberg numbers $We_1=\sqrt{\frac{a(u_w\Gamma)^2}{\upsilon}}$, $We_2=\sqrt{\frac{a(v_w\Gamma)^2}{\upsilon}}$, the stretching factor $A=\frac{b}{a}$, Hartmann number $M=\frac{\sigma B_0^2}{a\rho_f}$, mixed convection parameter $\lambda=\frac{g_t\,\beta}{a u_w}(1-C_\infty)\,(T_w-T_0)$, buoyancy ratio parameter $Nr=\frac{(\rho_p-\rho_f)(C_w-C_0)}{\beta\rho_f(1-C_\infty)\,(T_w-T_0)}$, bioconvection Rayleigh number $Rb=\frac{\gamma(\rho_m-\rho_f)(N_w-N_\infty)}{\beta\rho_f(1-C_\infty)\,(T_w-T_\infty)}$, the temperature ratio parameter $\theta_w=\frac{T_w}{T_\infty}$, Prandtl number $Pr=\frac{\nu}{\alpha}$, thermal radiation parameter $Rd=\frac{4\sigma^* T_\infty^3}{k_\infty k^*}$, Brownian motion parameter $Nb=\frac{\tau D_B(C_w-C_0)}{\nu}$, thermophoresis parameter $Nt=\frac{\tau D_T(T_w-T_0)}{\nu T_\infty}$, thermal relaxation parameter $\delta_T=a\Lambda_T$, solutal relaxation parameter $\delta_C=a\Lambda_C$, bioconvection Brownian motion parameter $Np=\frac{\tau D_N(N_w-N_0)}{\nu}$, Eckert number $Ec=\frac{(u_w)^2}{\rho c_{p(T_w-T_0)}}$, Lewis number $Le=\frac{\alpha}{D_B}$, chemical reaction rate $Cr=\frac{k_c}{a}$, bio-convection Schmidt number $Sb=\frac{\upsilon}{D_N}$, the constant microorganisms concentration difference parameter is $\Omega=\frac{N_0}{N_w-N_0}$, bio-convection Peclet number $Pb=\frac{mW_c}{D_N}$, thermal diffusivity $\alpha=\frac{k_\infty}{\rho c_p}$, the thermal stratified parameter $S_1=\frac{c_2}{c_1}$, mass stratified parameter $S_2=\frac{d_2}{d_1}$, and the stratification of microbial density parameter is $S_3=\frac{e_2}{e_1}$. The coefficients Lb_1 and Lb_2 in Eqs. (22) and (23) arise from the mixed streamwise–wall-normal cross-derivative terms within the Cattaneo–Christov thermal and solutal relaxation, representing the non-dimensional contribution of this cross-diffusion component to the streamwise-velocity–temperature and streamwise-velocity–concentration coupling. The constant δ^2 is a small shear-rate regularization parameter, introduced to prevent the derivative Carreau–Yasuda correction terms from becoming singular as $f''+g''=0$; its magnitude is negligible relative to the near-wall curvature terms it accompanies but is not vanishingly small relative to f''^2, g''^2 in the far-field region, where the correction term itself is already small in absolute magnitude.

The other interesting quantities of the model are the heat transfer rate (Nusselt number), drag function (Skin friction coefficients) for x and y directions, local Sherwood number, and the microbial density number. These engineering interest quantities are expressed as:

$$C_{fx}=\frac{\tau_{xz}}{\frac{1}{2}\rho u_w^2},\ C_{fy}=\frac{\tau_{yz}}{\frac{1}{2}\rho v_w^2},\ Nu_x=\frac{xq_w}{k(T_w-T_\infty)},\ Sh_x=\frac{xq_m}{D_B(C_w-C_\infty)},\ Nn_x=\frac{xq_n}{D_N(N_w-N_\infty)}. \tag{26}$$

Here stress tensor is denoted as τ_w, heat flux is q_w, mass flux is denoted by q_m, and the mathematical expressions of these terms are:

$$\begin{gathered}\tau_{xz}=\mu_0\left[1+(\tfrac{n-1}{d})(d+2)\Gamma^d\{(\tfrac{\partial u}{\partial z})^2+(\tfrac{\partial v}{\partial z})^2\}^{(\frac{d}{2})}\right]^{(\frac{n-1}{d})}\frac{\partial u}{\partial z}\bigg|_{z=0},\ \tau_{yz}=\mu_0\left[1+(\tfrac{n-1}{d})(d+2)\Gamma^d\{(\tfrac{\partial u}{\partial z})^2+(\tfrac{\partial v}{\partial z})^2\}^{(\frac{d}{2})}\right]^{(\frac{n-1}{d})}\frac{\partial v}{\partial z}\bigg|_{z=0},\\ q_w=-[K(T)]\tfrac{\partial T}{\partial z}|_{z=0}+(q_r)_w,\ q_m=-[D(T)]\tfrac{\partial C}{\partial z}|_{z=0},\ q_n=-D_N\tfrac{\partial N}{\partial z}|_{z=0}.\end{gathered} \tag{27}$$

The dimensionless form of the engineering quantities of drag function, heat transfer rate, and Sherwood number is mathematically written as:

$$\begin{aligned}C_{fx}\sqrt{Re_x}&=f''(0)\left[1+\left(\frac{n-1}{d}\right)(d+2)\left({We_1}^2\ f''^2+{We_2}^2\ g''^2\right)^{\left(\frac{d}{2}\right)}\right]^{\left(\frac{n-1}{d}\right)},\\ C_{fy}\sqrt{Re_y}&=g''(0)\left[1+\left(\frac{n-1}{d}\right)(d+2)\left({We_1}^2\ f''^2+{We_2}^2\ g''^2\right)^{\left(\frac{d}{2}\right)}\right]^{\left(\frac{n-1}{d}\right)},\\ Nu_x{Re_x}^{-1/2}&=-\theta'(0)\left[1+\frac{4}{3}Rd+4Rd(\theta_w-1)\theta(0)\right],\\ Sh_x{Re_x}^{-1/2}&=-\varphi'(0),\\ Nn_x{Re_x}^{-1/2}&=-\xi'(0).\end{aligned} \tag{28}$$

Here, the Reynolds numbers in x and y directions are defined as $Re_x=\frac{ax^2}{\nu}$, and $Re_y=\frac{ay^2}{\nu}$, respectively. The residual of the transformed non-linear ordinary differential equations Equ- (20-24) can be rewritten as:

$$\begin{aligned}\bar{F}=f'''&\left[1+\left(\frac{n-1}{d}\right)(d+2)\left({We_1}^2\ f''^2+{We_2}^2\ g''^2\right)^{\left(\frac{d}{2}\right)}\right]^{\left(\frac{n-1}{d}\right)}\\ &+\left[1+\left(\frac{n-1}{d}\right)(d+2)\left({We_1}^2\ f''^2+{We_2}^2\ g''^2\right)^{\left(\frac{d}{2}\right)}\right]^{\left(\frac{n-1}{d}\right)}\left\{\left(\frac{n-1}{d}\right)(d\right.\\ &\left.+2)\left({We_1}^2\ f''^2+{We_2}^2\ g''^2+\delta^2\right)^{\left(\frac{d-2}{2}\right)}f''[{We_1}^2\ f''f'''+{We_2}^2g''g''']\right\}\left[1+\left(\frac{n-1}{d}\right)(d+2)\left({We_1}^2\ f''^2+{We_2}^2\ g''^2\right)^{\left(\frac{d}{2}\right)}\right]^{-1}-(f')^2\\ &+f''(f+g)+A^2-M(f'-A)+\lambda(\theta-Nr\varphi-Rb\xi),\end{aligned} \tag{29}$$

$$\begin{aligned}\bar{G}=g'''&\left[1+\left(\frac{n-1}{d}\right)(d+2)\left({We_1}^2\ f''^2+{We_2}^2\ g''^2\right)^{\left(\frac{d}{2}\right)}\right]^{\left(\frac{n-1}{d}\right)}\\ &+\left[1+\left(\frac{n-1}{d}\right)(d+2)\left({We_1}^2\ f''^2+{We_2}^2\ g''^2\right)^{\left(\frac{d}{2}\right)}\right]^{\left(\frac{n-1}{d}\right)}\left\{\left(\frac{n-1}{d}\right)(d\right.\\ &\left.+2)\left({We_1}^2\ f''^2+{We_2}^2\ g''^2+\delta^2\right)^{\left(\frac{d-2}{2}\right)}g''[{We_1}^2f''f'''+{We_2}^2g''g''']\right\}\left[1+\left(\frac{n-1}{d}\right)(d+2)\left({We_1}^2\ f''^2+{We_2}^2\ g''^2\right)^{\left(\frac{d}{2}\right)}\right]^{-1}-(g')^2\\ &+g''(f+g)-Mg',\end{aligned} \tag{30}$$

$$\begin{aligned}\overline{\Theta}=&\left[1+\omega_1\theta+4Rd(\theta_w-1)\theta+\frac{4}{3}Rd\right]\theta''+[\omega_1+4Rd(\theta_w-1)]\theta'^2-Pr(S_1+\theta)\,f'+Pr(f+g)\,\theta'-Pr\delta_T(f+g)^2\theta''\\ &+2Pr\delta_T(S_1+\theta)Lb_1(f+g)f'\theta'-Pr\delta_T(S_1+\theta)(f')^2+Pr\delta_T(S_1+\theta)(f+g)f''-Pr\delta_T(f+g)(f'+g')\theta'\\ &+Pr\left[Nb\theta'\varphi'+Nt\theta'^2+Np\theta'\xi'\right]+PrEcM(f'^2+g'^2)+PrEc\left[1+\left({We_1}^2\ f''^2+{We_2}^2\ g''^2\right)^{\left(\frac{d}{2}\right)}\right]^{\left(\frac{n-1}{d}\right)}(f''^2+g''^2),\end{aligned} \tag{31}$$

$$\bar{\Phi}=\varphi''+Le(1+\omega_2\varphi)\varphi''+\omega_2Le\varphi'^2+(\tfrac{Nt}{Nb})\theta''-LePr(S_2+\varphi)\,f'+LePr(f+g)\varphi'-LePr\delta_C(f+g)^2\varphi''+2LePr\delta_C(S_2+\varphi)Lb_2(f+g)f'\varphi'- \tag{32}$$

$$LePr\delta_C(S_2+\varphi)(f')^2 + LePr\delta_C(S_2+\varphi)(f+g)f'' - LePr\delta_C(f+g)(f'+g')\varphi' - LePrCr\varphi,$$

$$\bar{\xi} = \xi'' + Sb(f+g)\xi' - Sb(S_3+\xi)\,f' + \left(\frac{Nt}{Np}\right)\theta'' - Pb[\xi'\varphi' + (\Omega+\xi)\varphi'' + S_3\varphi'']. \tag{33}$$

3. Physics-Informed Neural Network

This work develops a Physics-Informed Neural Network model integrating the physical laws of the governing equations. A fully connected neural network is applied in the PINN architecture, as shown in Fig. 2, with the input, output, and hidden layers with automatic differentiation (AD) and the residual of the governing equations. The input layer has one neuron of the similarity variable, while the output layer consists of 5 neurons representing the velocity in the x and y-directions, temperature, concentration, and microbial concentration of the model. The AD is used to compute the derivatives of these variables to calculate the residuals of the ODEs of the considered model.

The PINN architecture is constructed by minimizing a composite loss function consisting of the governing differential equation residuals and associated boundary conditions. The transformed ordinary differential equations are embedded into the training process of a deep neural network to approximate the solution fields without requiring labeled data. The model utilizes only collocation points within the computational domain and prescribed boundary constraints.

The PINN employs a multilayer perceptron (MLP) architecture with one input layer, five fully connected hidden layers containing 128 neurons each, and an output layer corresponding to the solution variables. The hyperbolic tangent ($tanh$) activation function is used in all hidden layers to capture the nonlinear behaviour of the governing equations. The total number of trainable parameters (weights and biases) is $66{,}949$, providing sufficient representational capacity for approximating the coupled solution fields and their derivatives.

The goal is to learn fields $y(\eta;\ p) =\ f, g, \theta, \varphi, \xi]$ and their derivatives for parameter vectors p comprising We_1, We_2, A, M, λ, Nr, Rb, θ_w, Pr, Rd, Nb, Nt, δ_T, δ_C, Np, Ec, Le, Cr, Sb, Ω, Pb, S_1, S_2, S_3. A Physics-Informed Neural Network (PINN) to solve for y by minimizing physics residuals of the PDEs and boundary conditions over collocation points in $\eta \in [0, \eta_{max}]$, with adaptive sampling near boundary layers and far-field regions:

$$NN(\eta; p) \equiv [f, g, \theta, \varphi, \xi; \Theta_p]. \tag{34}$$

denotes the PINN with automatic differentiation (AD) and the trainable parameter Θ_p for biases and weights. These weights and biases are updated iteratively via the $Adam$ optimizer, with an exponentially decaying learning rate starting at 0.001, ensuring stability and convergence over $20{,}000$ epochs. Here p denotes the fixed set of physical parameters at which this particular network is trained $(We_1, We_2, A, M, \lambda, Nr, Rb, \theta_w, Pr, Rd, Nb, Nt, \delta_T, \delta_C, Np, Ec, Le, Cr, Sb, \Omega, Pb, S_1, S_2,\ S_3)$, not an input to the network consistent with the single-neuron input layer in Table 1, the trained $NN(\eta; p)$ takes only η as input, and evaluating the model at a different parameter set requires retraining rather than a forward pass with a new p.

This suggested architecture is completely data-independent since no solution data are provided for the purpose of training. Rather, the network weights are tuned by minimizing residuals of the governing equations and the boundary conditions at the collocation points. This data generation for the PINN model relies on producing collocation points throughout the normalized domain, including dense placements near boundary layers and in far-field regions, to efficiently sample the solution space for the 3D bioconvective Carreau-Yasuda nanofluid equations. At each collocation point, the network predicts solution variables (velocity, temperature, concentration, and microorganism density), with their spatial derivatives computed automatically via automatic differentiation. This process enables direct substitution into the system's coupled nonlinear ODEs, yielding physics residuals at every location in the domain.

To enforce both the governing equations and boundary conditions, the loss function for our PINN combines two principal components: the mean squared residual of the ODEs throughout the interior domain ($\mathcal{L}_{ODE}$) and the mean squared residual of the boundary conditions ($\mathcal{L}_{BC}$). Total loss is expressed as:

$$\mathcal{L}_{Total} = \lambda_{ODE}\ \mathcal{L}_{ODE} + \lambda_{BC}\mathcal{L}_{BC}. \tag{35}$$

Here, $\lambda_{ODE} = 0.1$ and $\lambda_{BC} = 0.5$ are the fixed weights assigned to the ODEs and BCs. Where,

$$\mathcal{L}_{ODE} = \frac{1}{N_f}\sum_{i=1}^{N_f}\left|\mathcal{N}\left[\hat{u}_{\Theta_p}(x_i)\right] - f(x_i)\right|^2, \tag{36}$$

$$\mathcal{L}_{BC} = \frac{1}{N_b}\sum_{i=1}^{N_b}\left|\mathcal{B}\left[\hat{u}_{\Theta_p}(x_i)\right] - f(x_i)\right|^2. \tag{37}$$

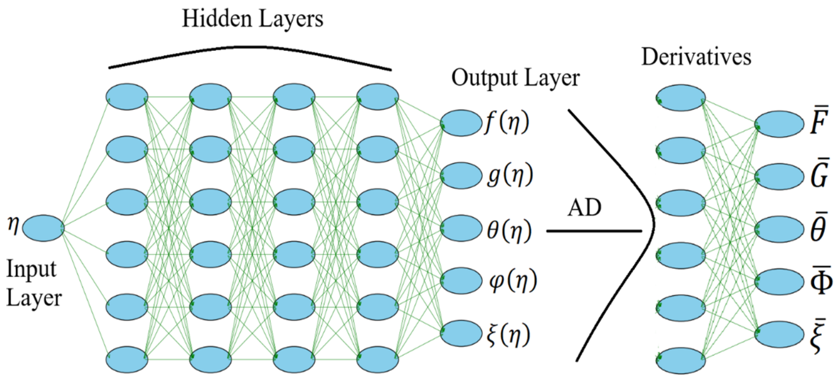

Fig. 2. PINN architecture for the bioconvective Carreau-Yasuda model.

Table 1. PINN training summary.

Component	Value
Network Architecture	Fully connected MLP $[1,128,128,128,128,128,5]$
Total Trainable Parameters	$66{,}949$
Activation Function	Hyperbolic tangent $tanh$
Optimizer	$Adam$
Initial Learning Rate	1×10^{-3}
Final Learning Rate	3.77×10^{-4}
Training Epochs	$20{,}000$
Interior Collocation Points	$3{,}000$
Boundary Points	200
Final Total Loss	1.94×10^{-4}
Training Time	$1660.6s(CPU)$
Programming Language	Python 3.11
Deep Learning Framework	TensorFlow 2.18.0
Hardware	Intel Core i7-12700H CPU, 32 GB RAM

Here, the differential operator of the PDEs is represented by $\mathcal{N}[\bullet]$, while the boundary conditions are denoted by $\mathcal{B}[\bullet]$. The number of interior collocation points for the ODEs is denoted by N_f, while the total number of boundary points is denoted by N_b. The Adam optimization algorithm is utilized to minimize the total loss $(\mathcal{L}_{Total})$ by optimizing the neural network parameters Θ_p. This confirms that the solutions generated by the PINNs are physically consistent with the bioconvective Carreau-Yasuda model and satisfy all boundary constraints to high precision.

The training of PINNs employs an adaptive sampling strategy to capture the complex solution efficiently features across the domain. These considered collocation points are based on the idea is to capture the complex phenomena of the fluid near the wall (at the surface), over the surface, and within the boundary layer to understand the changes, and in the ambient to observe the asymptotic behaviour. The 70% of the collocation points are uniformly distributed over the entire surface, while 20% collocations points are within the boundary layers, and the final 10% points are distributed far from the wall. This adaptive collocation sampling approach enhances the learning efficiency of the PINNS by attaining the physically critical areas of the model.

The present implementation uses the Adam optimizer throughout training, without a subsequent second-order refinement stage. The training diagnostics indicate the loss had not met a strict convergence criterion by epoch $20{,}000$ (convergence ratio $\sigma/\mu = 1.92$ over the final 100 epochs, against a target of < 0.05), with residual epoch-to-epoch fluctuations persisting even late in training. A second-order refinement stage such as L-BFGS, applied after the Adam phase, would be expected to reduce these late-stage oscillations and tighten the final residual levels, and is identified as a concrete direction for improving convergence in future work. The optimization process monitored the evolution of data, physics, and boundary losses to ensure stable convergence. The architecture and training setup used for the PINN model are presented in Table 1. The network architecture is based on a multilayer perceptron with fully connected layers that have five hidden layers with 128 neurons each, and a hyperbolic tangent activation function. The training process involved the use of $20{,}000$ iterations with a decaying learning rate between 10^{-3} to 3.77×10^{-4} using the Adam optimizer. This was done by employing $3{,}000$ interior collocation points and 200 boundary points to attain a loss of 1.94×10^{-4} in $1660.6\ s$ of CPU computation.

This PINN model is constructed with the similarity variable as the input to the multilayer perceptron (MLP) network, by reducing the dimensionality of the problem and leveraging the self-similar behavior inherent in the boundary layer and bioconvective flows. Using the similarity variable as input to a MPL has an advantage over using the spatial and temporal variables as input by making PINNs to understand the solution fields as a function of the similarity variable instead of two different variables of spatial and temporal. By using the similarity variable as input, the network streamlines learning of the velocity components, temperature, concentration, and microorganism density profiles with a small yet sufficiently rich input space.

The output layer generates the necessary physical fields. This approach simplifies the training procedure and enhances generalization across the physical domain. Automatic differentiation then facilitates the evaluation of the necessary spatial derivatives with respect to the similarity variable to impose the governing coupled ODEs as physics-informed constraints within the loss function. The integration of annotations on the boundaries, transitional, and far-field zones give the physical context in which the PINN predicts very low errors when compared to regions of steep gradients of the solution fields or when the solution field is asymptotic. These residual distributions confirm the effectiveness of the PINN in learning and enforcing the governing multiple coupled nonlinear PDEs that predict the flow of bioconvective nanofluids through Carreau-Yasuda-like flow scenarios.

4. Results and Discussion

This investigation aims to develop a Physics-Informed Neural Network (PINN) framework with SQLM data and without data to solve, infer, and generalize the three-dimensional, MHD Carreau–Yasuda nanofluid boundary-layer flow problem with dual (thermal and solutal) variable conductivities, triple stratification (thermal, solutal, microbial), quadratic thermal radiation, chemical reaction, and bioconvection. The outcomes of this study are as follows:

The evolution of training losses indicates a monotonic reduction of the total loss from 0.5787 at epoch 200 to 0.0953 at epoch 2000. The gradual decrease in data, physics, and boundary residual components demonstrates stable optimization without divergence or oscillatory behaviour.

Figure 3 represents the characteristics of the velocity components, temperature, solute concentration, and microorganism density profiles, revealing essential boundary layer structures and fluid rheology. The velocity profiles f (streamwise) and g (transverse) in Fig.3(a) show the classical boundary layer characteristics with smooth monotonic decay from no-slip wall conditions, indicating proper capture of shear-thinning/thickening behaviors governed by Carreau-Yasuda parameters n and d.

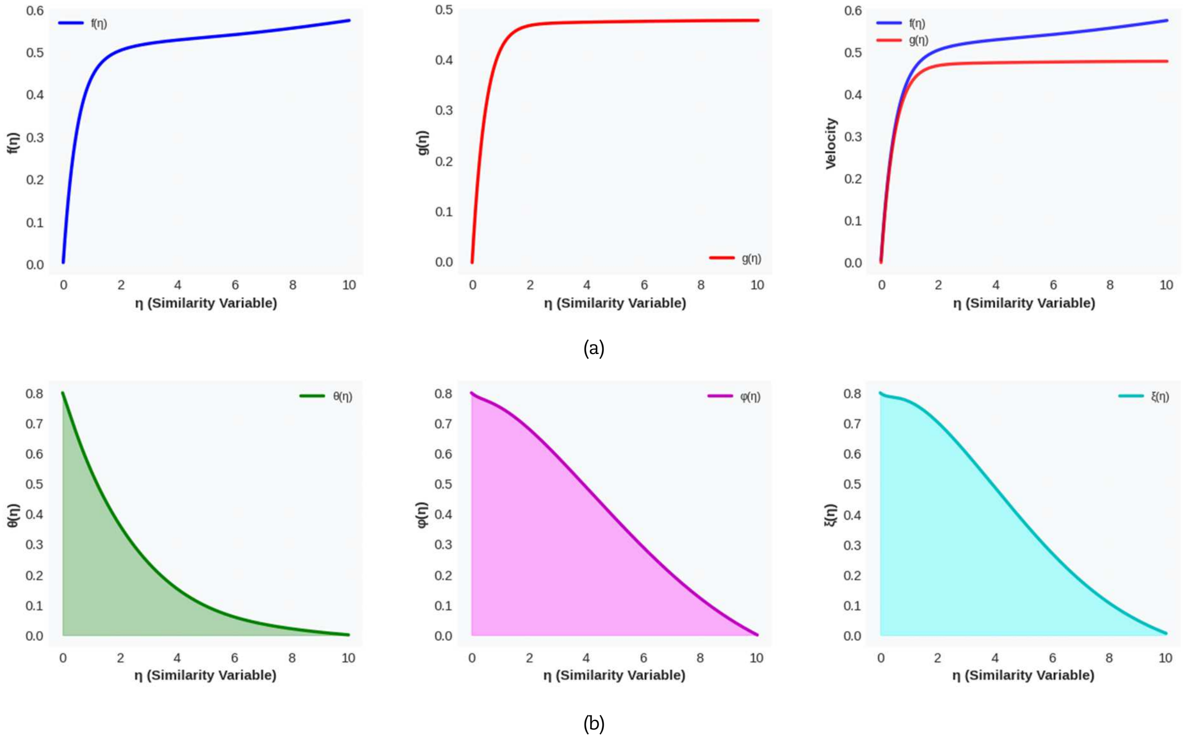

Fig. 3. (a) Velocity profiles, (b) Temperature, solutal, and microbial concentration profiles.

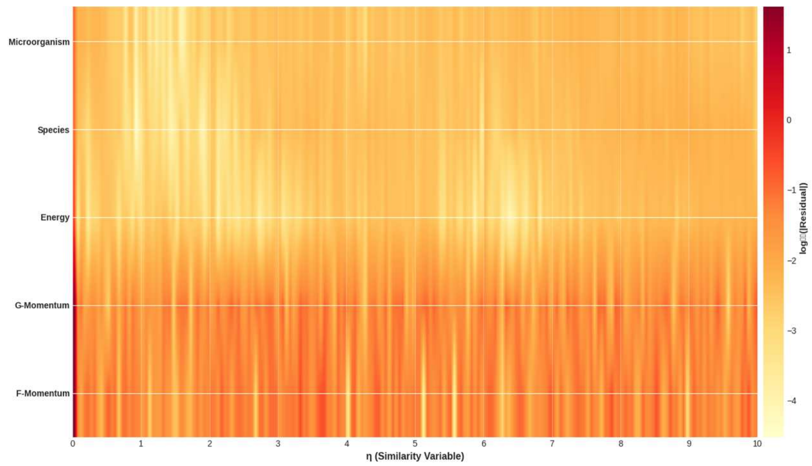

Fig. 4. PDE residuals heatmap plot.

The temperature θ, concentration φ, and microorganism ξ profiles highlight thermal and mass transport layers with expected asymptotic approach to far-field values, consistent with Prandtl, Schmidt, and Lewis number influences in Fig. 3(b). The variation of the boundary layer thickness in these plots confirms the relative saturation depths uttered by fluid and transport parameters. These plots demonstrate the PINN's adaptability and physical reliability in reproducing complex non-Newtonian fluid characteristics and emphasizing the changes in viscoelastic parameters and dimensionless groups that influence the flow and transport phenomena, widely used in engineering design and biomedical applications.

The residual heatmap provided in Fig. 4 shows a critical diagnostic of the PINN's solution fidelity. The colour intensity, representing the logarithm of the residual magnitudes, reveals how well the physics-informed neural network satisfies each equation at different points in the domain. The lower residual values (shown by lighter colours) indicate that the PINN is effectively capturing the complex momentum transport associated with the flow of the non-Newtonian Carreau-Yasuda nanofluid. While the moderate energy residual values indicate good but slightly less precise enforcement of the energy conservation governing temperature fields, because of the typical nonlinear coupling in thermal transport and fluid flow. Moreover, very low residual magnitudes for species concentration and microorganism density confirm strong accuracy in modelling mass transport and bioconvection phenomena, critical for capturing microorganism dynamics alongside nanoparticle dispersion. This plot confirms that the PINN solution adheres well to the underlying PDEs throughout the domain, with very minimal violations, showing confidence in the physical realism, numerical stability, and predictive capability of the PINN in modelling this intricate multiphysics system.

The graphs in Fig. 5, showing a statistical analysis of partial differential equation (PDE) residuals provides critical insight into the fidelity and robustness of the PINN solution for the 3D bioconvective Carreau-Yasuda nanofluid model. The histograms, boxplots, cumulative distribution curves, and a summary statistics table show that PINNs satisfies the governing equations for the momentum equations in the x and y directions, energy, species concentration, and microbial concentration transfer across the computational domain.

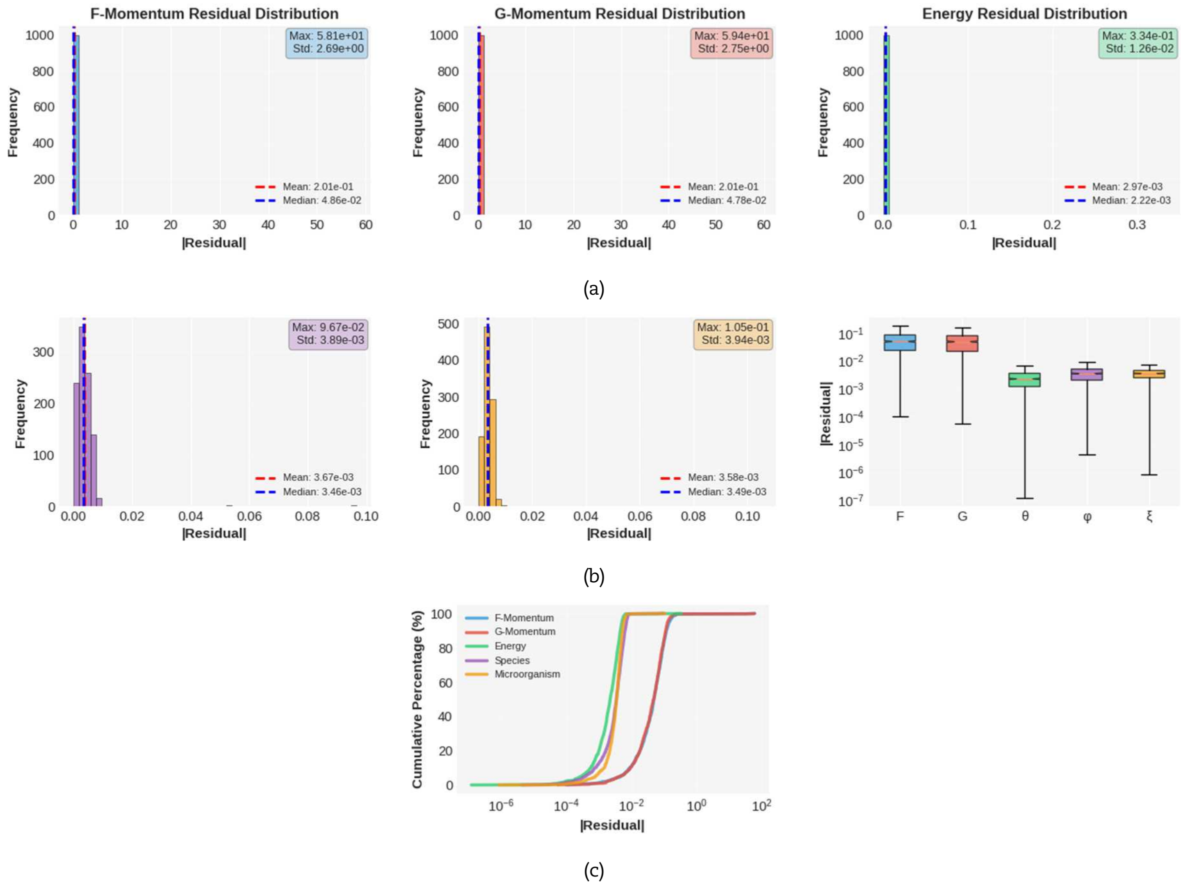

Fig. 5. (a) Velocity and temperature residual profiles, (b) Species and microbial concentration residual profiles, (c) Cumulative residual distribution plot.

The residual histograms and cumulative distributions in Fig. 5(a), and Fig. 5(b) for F-momentum, G-momentum, energy, species, and microorganism equations all demonstrate highly skewed distributions sharply concentrated near zero, with only a few rare, larger outliers. The formulation of both the mean and standard deviation for each individual set of residuals shows notable reductions compared to traditional methods, especially with respect to the energy, species, and microorganisms, thus demonstrating the high fidelity of the PINNs' ability to enforce conservation laws. The majority of all equations have their respective boxplots indicating that nearly all of the residuals are concentrated around a median of zero, while the momentum equations have the occasional high outlier, indicating the presence of localized complexity in the solutions or abrupt changes in the gradient, which may be made apparent through the use of more site-specific sampling or refinement to the network.

The overall presentation of the results in Table 2 and Fig. 5(c) corroborates the above findings by presenting a quantitative measure of the mean, median, maximum, and root mean square (RMS) for each of the residuals of the equations examined. The low RMS and very small global means reflect strong numerical accuracy and physical consistency in all areas of the solution domain. Together, these results lend strong support to the reliability of the PINN method for developing an accurate approximation for this challenging multi-physics problem and demonstrate how capable the network is at producing physically representative fields for velocity, temperature, concentration, and microorganisms. While there are naturally some outlying residuals due to the nonlinear nature, as well, of the coupled PDEs under investigation, the limited and small frequency of outlying residuals illustrates the appropriateness of this current model and methodology for advanced engineering and applied physics purposes. Thus, the extensive residuals analysis provides strong quantitative evidence in support of the integrity and predictive effectiveness of the PINN solutions.

The spatial distribution of residuals for governing PDEs, supported by informative legends, statistical annotations, and a combined residual plot on a log scale, is depicted in Fig. 6. Figure 6(a) shows the spatial distribution of residuals for the F-momentum and G-momentum equations across the similarity variable η. Residual values remain consistently low throughout the domain, with a few localized spikes indicating high-gradient regions near the boundary layer. The maximum residual of approximately 53 is confined to initial points, suggesting effective momentum equation enforcement elsewhere. This demonstrates the model's strong capacity to satisfy momentum conservation in the primary flow direction under complex non-Newtonian rheology. Similarly, the G-momentum residual plot has most residuals near zero and few outliers located at low η. This confirms accurate resolution of secondary flow effects and lateral momentum transfer. The localized spikes emphasize crucial regions that demand fine sampling and network adaptation to capture nuanced flow behavior.

Table 2. Summary table of PINN outcomes.

Equations	Mean	Median	Max	Std. Dev	RMS
F-Momentum	2.0068e-01	4.8597e-02	5.8087e+01	2.6862e+00	2.6937e+00
G-Momentum	2.0105e-01	4.7790e-02	5.94434e+01	2.7493e+00	2.7566e+00
Energy	2.9730e-03	2.2162e-03	3.3391e-01	1.2646e-02	1.2991e-02
Species	3.6682e-03	3.4590e-03	9.6652e-02	3.8856e-03	5.3436e-03
Microbial	3.5846e-03	3.4880e-03	1.0518e-01	3.9419e-03	5.3280e-03

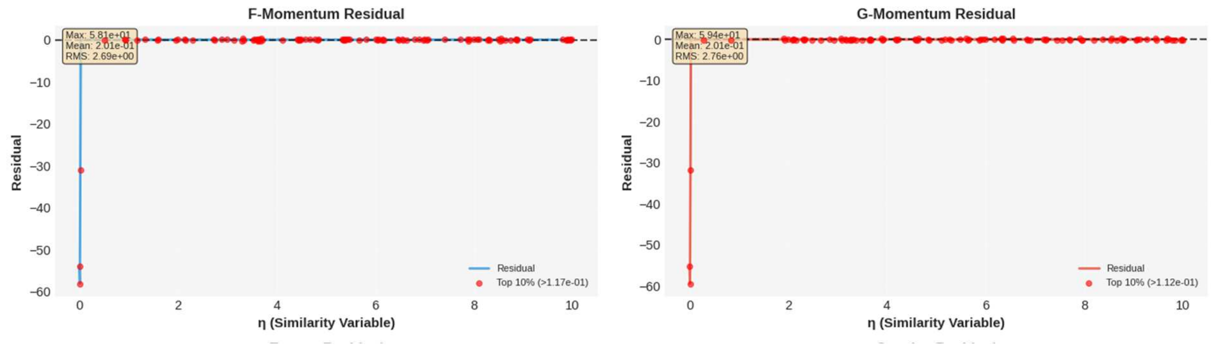

(a)

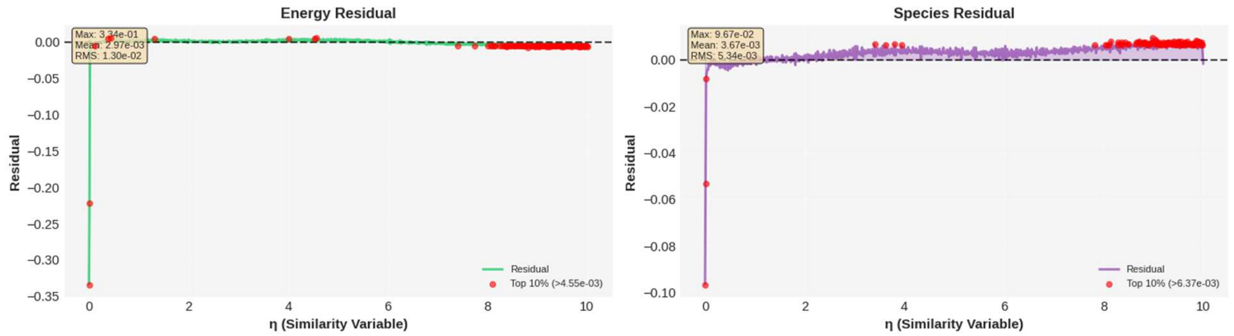

(b)

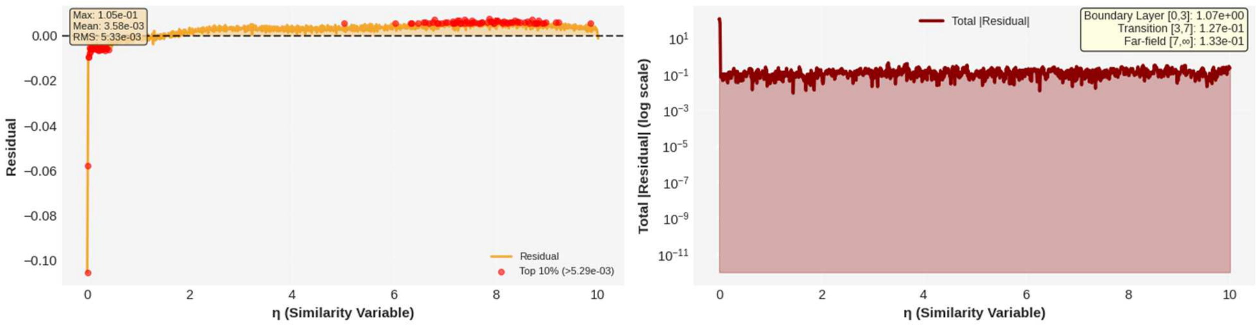

(c)

Fig. 6. (a) Momentum residuals plot, (b) Temperature and concentration plots, (c) Microbial residual and combined plot.

The energy and species concentration residual plots are shown in Fig. 6(b). The energy residual's magnitude is comparatively smaller than the values of the momentum residuals, while the tendency towards zero values dominates the domain with minor deviations of the magnitude towards the positive at a small similarity variable η. The energy residual plot confirms the reliability of PINNs' heat transfer and thermal energy management. The species residual distribution shows a slight increase in the lower values of the similarity variable and forms a cluster near zero. This again confirms the learning efficiency of PINNs in mass transfer and mass conversion.

The microorganism residual plot follows a similar trend to species residuals with very low residuals throughout the domain, as reflected in Fig.6(c). Slightly higher values near $\eta = 0$ align with biologically active boundary layers, reflecting the model's detailed capture of bioconvective microorganism transport and associated complex reactions or diffusion near boundaries. The final plot aggregates the total residual magnitude on a logarithmic scale. It illustrates that combined residuals remain within four orders of magnitude across the domain, highlighting overall consistency and convergence stability. It demonstrates that the residuals generated by the solution of the governing PDEs do not exceed four orders of magnitude from the boundary to the flow domain, indicating convergence stability. The annotations defining boundary, transition, and far-field layers provide physical context, showing that the PINN maintains low predicted errors even in critical regions where gradient changes are steep or solution fields asymptote. Collectively, these spatial residual distributions validate the PINN's effective learning and enforcement of multiple coupled nonlinear PDEs governing Carreau-Yasuda bioconvective nanofluid flow.

The comprehensive training performance analysis presented in Fig. 7(a) systematically characterizes the progression and stability of the training process for the PINN. The main loss evolution plot illustrates the decrease of total loss, ODE loss, and boundary condition loss over 20,000 epochs, segmented into distinct training phases such as rapid descent, refinement, and convergence. The rapid initial loss reduction highlights the neural network's quick learning of the governing PDE constraints and boundary conditions; the later plateau and oscillations reflect convergence toward an optimal but non-trivial PDE solution.

The loss reduction rate plot in Fig. 7(b) shows ongoing learning progress with mostly negative values, indicating steady loss decline despite local oscillations. This loss component breakdown plot emphasizes that ODE residuals dominate the total loss throughout training, while boundary condition loss remains comparatively lower but consistent, indicating effective simultaneous enforcement of all physical constraints.

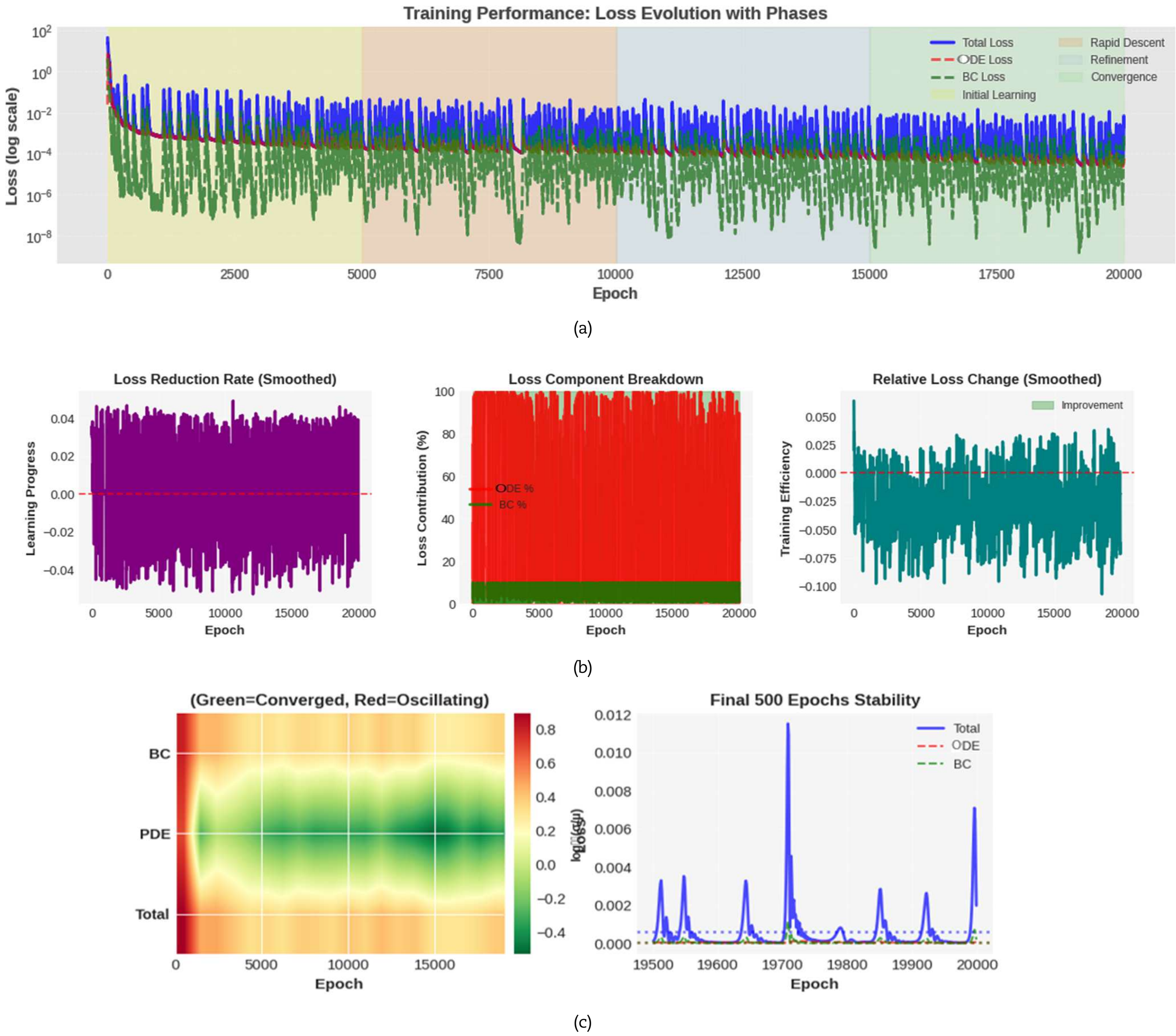

Fig. 7. (a) Loss Evolution of PINN, (b) Training performance analysis, (c) Convergence and stability analysis of the training process.

The relative loss change plot in Fig. 7(c) tracks smoothed training efficiency, showing incremental improvements with minor fluctuations, affirming continued network refinement. The convergence quality heatmap provides spatiotemporal diagnostics of the loss components via a green-yellow-red colour scale, where green bands signify epochs and phases of steady, robust convergence, while occasional red regions indicate transient oscillatory behavior primarily in boundary condition losses, reflective of model adjustment to boundary constraints. The final 500-epoch stability plot zooms into late training phases, demonstrating oscillatory but diminishing losses with some spiking ODE residuals, consistent with complex nonlinearities and the neural optimizer's iterative updates.

This plot from Fig. 8(a) presents the streamlines formed by the primary velocity component (f), and streamlines defined by the transverse velocity component (g) mapped over the similarity variable and streamwise direction. For the f-plot, the lines are smooth and concentrated near the wall and boundary layer regions, confirming strong wall-driven shear and momentum transport. The colour-coded velocity scale reveals regions of higher fluid speed close to the wall, decaying monotonically as the distance increases, indicating efficient dissipation of flow energy into the domain. For the g-plot, the streamline patterns show secondary flows and weak vortices superimposed on the primary field, especially in the mid-domain. The lower magnitude colour scale highlights areas where crosswise momentum transport is effective, contributing to mixing and recirculation necessary for bioconvective and non-Newtonian dynamics. These plots demonstrate the non-Newtonian boundary layer behavior characteristic of Carreau-Yasuda fluids with well-resolved gradients.

Figure 8(b) overlays the velocity magnitude as a colormap beneath the black streamlines, enabling direct assessment of regions where speed is highest and flow is most vigorous. The peak values are near the wall, supporting the previous findings, while the smooth transition toward lower velocities signal stable transport into far-field regions. The detail in streamline curvature and colour gradient facilitates interpretation of the main transport pathways and the zones where boundary layer diffusion dominates, confirming the accuracy of neural network predictions. The other plot superposes vorticity, an indicator of rotational flow and mixing with flow streamlines. Vorticity is highest near the wall and central regions, where gradients in velocity components are steepest. The presence of blue-shaded zones with tightly packed streamlines suggests strong mixing and enhanced bioconvective effects in those areas. This plot reveals the local dynamics crucial for nanoparticle and microorganism transport, and the overall agreement with velocity patterns demonstrates the physical consistency and completeness of the PINN-generated solution.

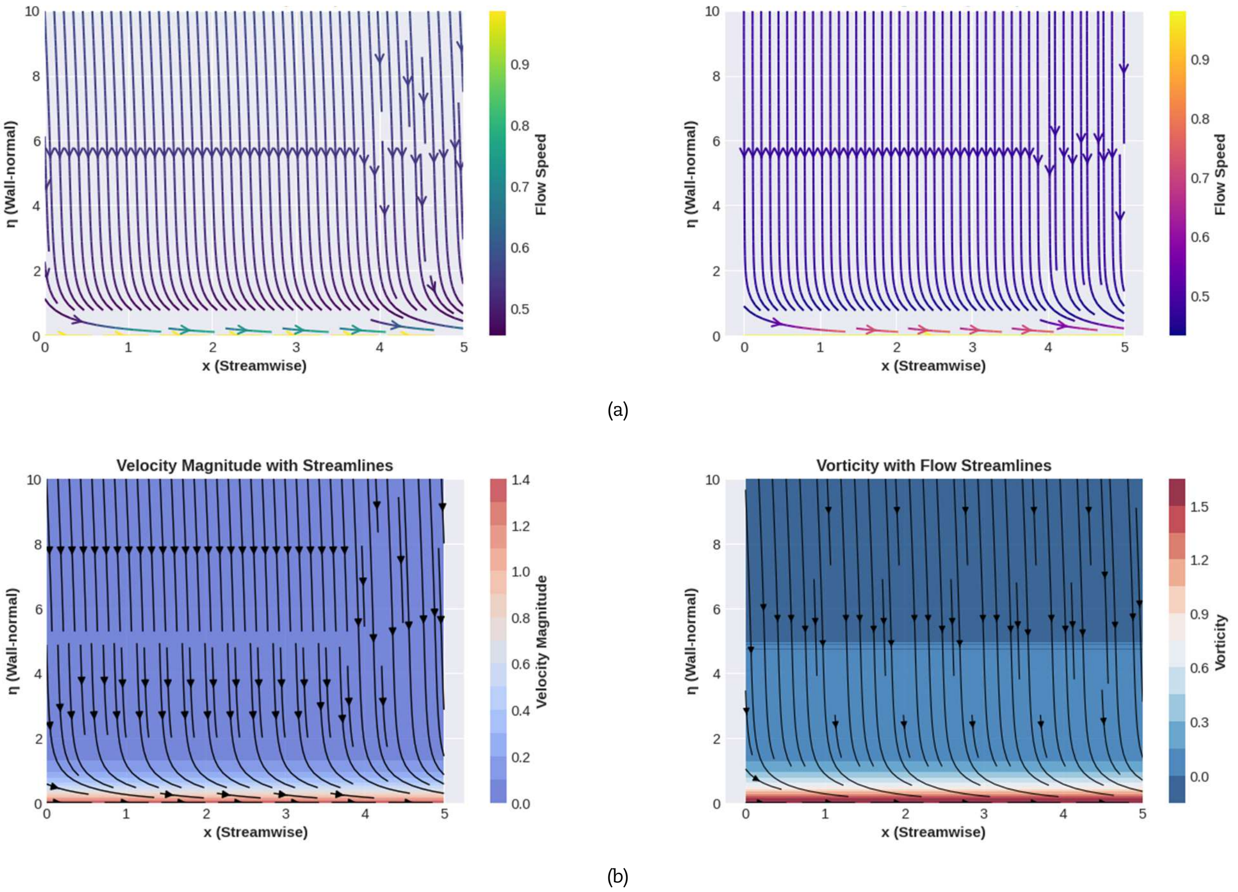

Fig. 8. (a) Streamwise plots for the velocity profiles, (b) Streamline profiles.

The training loss evolution graph in Fig. 9(a) provides a detailed assessment of the PINN model's optimization process across 20,000 epochs. The plot displays the trajectories of the total loss (black), the ODE residual loss (blue), and the boundary condition loss (red) on a logarithmic scale. The initial phase shows a steep reduction in all loss components, reflecting rapid improvement as the network assimilates the governing equations and enforces boundary conditions. Beyond this rapid descent, the losses progressively decrease at a slower rate, exhibiting lower-magnitude oscillations characteristic of stochastic neural optimization in complex, high-dimensional solution spaces. Notably, both ODE and boundary condition losses stabilize to values several orders of magnitude lower than their initial states, evidencing strong adherence to the physical constraints imposed by the coupled equations of the system. The comparatively lower and highly fluctuating boundary condition loss relative to the ODE loss indicates that the model consistently maintains accurate boundary condition enforcement, focused on minimizing the more demanding residuals associated with the nonlinear ODEs. The final total loss of training reached approximately 1.94×10^{-4}, where the ODE residual loss contributed about 5.313×10^{-4}, and the boundary condition loss (BC loss) accounted for 1.921×10^{-4}. This distribution indicates that the PINN effectively enforced both the governing equations and the prescribed boundary constraints, and the smooth evolution of all loss components confirmed the stability and accuracy of the optimization process, as illustrated in Fig. 9(a). The low residual levels demonstrate that the trained PINN successfully captured the coupled nonlinear physics of the 3D Carreau–Yasuda nanofluid model without requiring any labeled data. The eventual convergence and sustained low magnitude of all loss values support the reliability and robustness of the training strategy, confirming that the PINN has achieved a high-quality, physically meaningful solution for the bioconvective Carreau-Yasuda nanofluid problem.

The total loss, as well as the decomposition into physical ODE loss, is illustrated in Fig. 9(b), and boundary condition (BC) loss across training epochs is shown in Fig. 9(c). Initially, the sharp drop in total and ODE losses signifies rapid fitting of the neural network to the governing equations and boundary conditions, ultimately stabilizing at a value significantly lower than its starting point. This behavior confirms that the neural network is consistently improving its representation of the governing equations and achieving high physical fidelity. In later epochs, the plateau and small oscillations suggest slower fine-tuning as the PINN converges on a near-physical solution. The minimal value of the final losses indicates a strong adherence to the PINN model for learning the physics and characteristics of the Carreau-Yasuda nanofluid model.

The bar graph from Fig. 10 presents the engineering quantities evaluated at the wall $(\eta = 0)$, showing a comparative snapshot of fluid dynamic and transport performance for the bioconvective Carreau-Yasuda nanofluid model. The chart displays drag function (skin friction) coefficients in both the streamwise (i.e., x-direction) $C_{fx}\sqrt{Re_x}$ and transverse directions (i.e., y-direction) $C_{fy}\sqrt{Re_y}$, with the local Nusselt number $Nu_x/\sqrt{Re_x}$, local Sherwood number $Sh_x/\sqrt{Re_x}$, and biomass transfer number $Nn_x/\sqrt{Re_x}$. The direction of the drag function coefficients show that resistance from non-Newtonian boundary layers is also made possible through continuous momentum transfer from fluid to wall. In contrast to drag coefficients, local Nusselt numbers reflect efficient heat transfer, while local Sherwood and microbial density number values are both positive, indicating strong mass and microorganism transport at the interface. These results show that the PINN model has accurately represented key surface phenomena, confirming both non-Newtonian shear effects as indicated by negative skin friction, as well as active thermal and bioconvective mechanisms at the wall due to positive transfer numbers. This concise bar representation of drag, Nusselt, Sherwood, and microbial density number values will provide an intuitive understanding of the physical principles involved and quantitatively demonstrate how flow regime, rheology, and boundary conditions affect engineering behaviour in the simulated system.

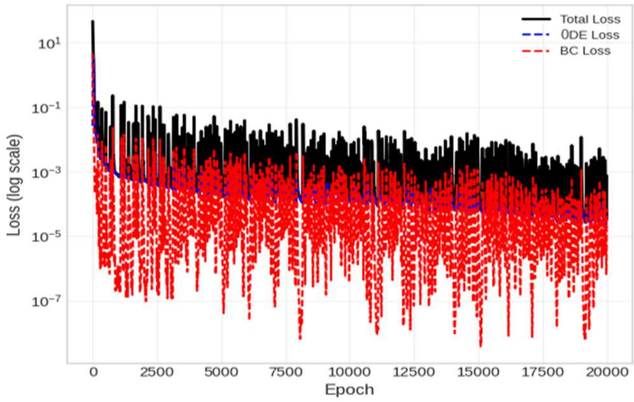

(a)

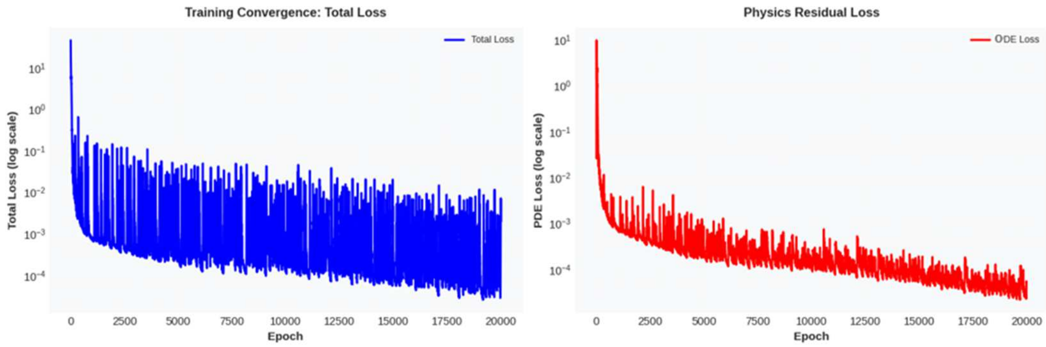

(b)

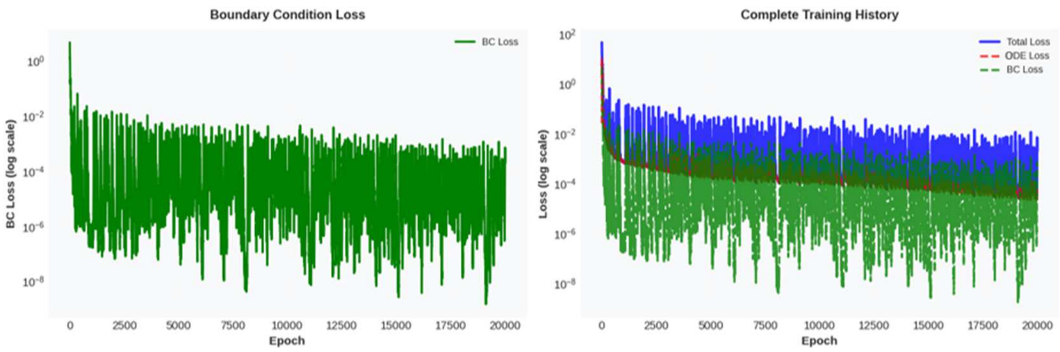

(c)

Fig. 9. (a) PINNs training performance, (b) Total and PDE loss plots, (c) BC and training history loss plots.

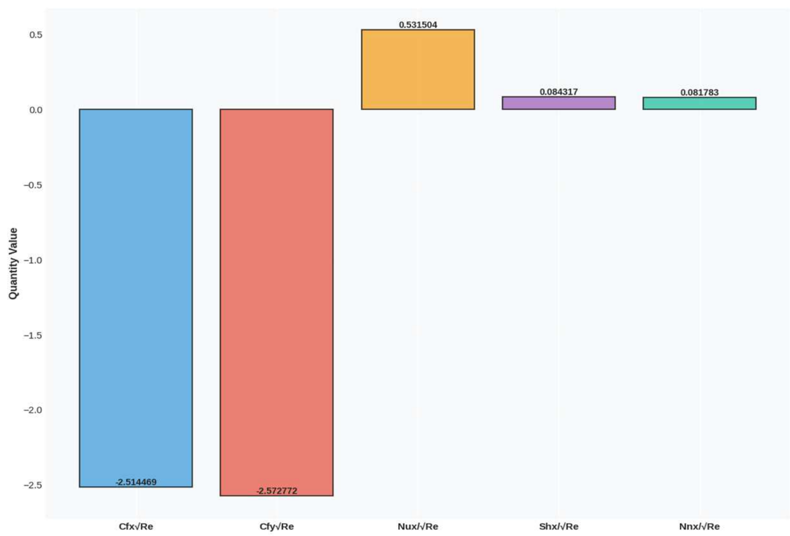

Fig. 10. Engineering quantities at the surface.

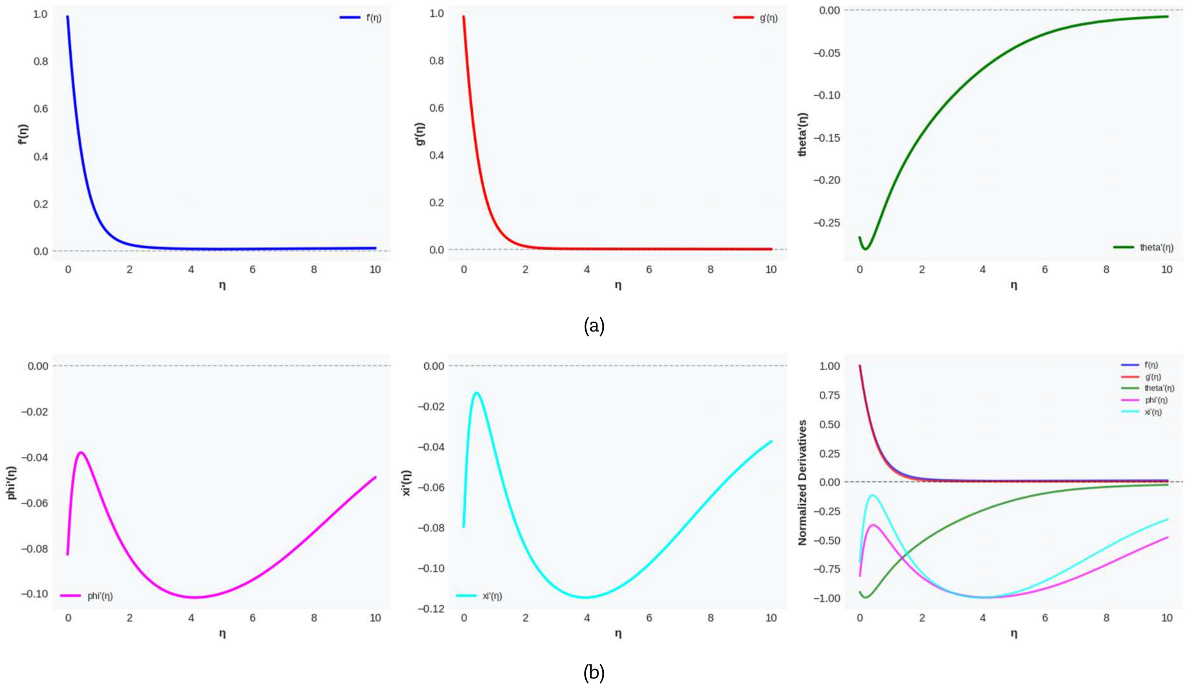

Fig. 11. (a) Velocity and temperature gradient analysis, (b) Species and microbial concentration gradient analysis.

The gradient of all the distributions of the model is shown in Fig. 11. The behavior of the transverse velocity gradients, $f'(\eta)$, $g'(\eta)$, and the temperature gradient $\theta'(\eta)$, across the boundary layer is depicted in Fig. 11(a). The velocity gradients in the x-direction and y-direction both initiate at unity at the boundary and exhibit a sharp, monotonic decay towards zero as η increases. This rapid decrease signifies that the fluid velocity quickly approaches the free-stream value, confirming that the momentum boundary layer is very thin and efficiently contained within η~4. The thermal gradient, θ', begins with a negative value at the wall, which is consistent with heat transfer from the wall to the fluid (cooling effect). As η increases, the temperature gradient increases monotonically, passing through zero and asymptotically approaching zero from the positive side in the far field. The maximum absolute value of the temperature gradient occurs at the surface, indicating the highest rate of heat transfer (local Nusselt number) is concentrated directly at the boundary, a characteristic finding in systems dominated by surface heating or cooling.

Figure 11(b) focuses on the gradients associated with mass and species transfer, i.e., the concentration gradient, $\varphi'(\eta)$, and the microorganism gradient, $\xi'(\eta)$. Both gradients exhibit a complex, non-monotonic profile, beginning at a negative value at the wall and asymptotically approaching zero in the free stream. The concentration gradient displays an initial rapid decrease to a minimum (most negative) value around η~1.5 before gradually increasing towards the far-field condition. This suggests a region of maximum concentration flux slightly away from the boundary. Similarly, the microorganism gradient shows a pronounced minimum at approximately η~1.5, but it also exhibits an initial anomalous peak slightly above the zero line near η~0.5 before plunging to its minimum. This unusual initial behavior is highly characteristic of bioconvection phenomena, where the combined effects of Brownian motion and thermophoresis induce a localized initial accumulation or redistribution of motile microorganisms near the surface. These profiles confirm that while mass and species are transferred from the boundary into the fluid, the mechanisms driving this transfer in the concentration and microorganism fields are significantly more complex and non-linear than the momentum and heat transfer processes.

The boundary condition validation for the velocity in the x-direction is shown in Fig. 12(a). This velocity validation shows viable agreement between the predicted and prescribed boundary conditions. At $\eta = 0$, the model enforces the no-slip condition $f(0) = 0$ with minimal error ($\approx 3.2 \times 10^{-3}$) and achieves near-perfect matching of the wall velocity gradient $f'(0) = 1$ within $\sim 1.36\%$ error. This confirms the ability of PINNs to accurately capture the streamwise velocity profile near the wall, a critical feature for shear-driven flow characterization. While the 1.36% deviation in $f''(0)$ reflects the precision of boundary-condition enforcement during training, it does not directly determine the error in the skin friction coefficient, since skin friction coefficients depends on $f''(0)$ rather than $f'(0)$. The actual impact on this engineering quantity is quantified directly in Table 4, where the PINN and SQLM values of drag function coefficients differ by only 0.08%, indicating that the boundary condition-matching error does not propagate substantially into the reported skin friction prediction for this parameter set.

The boundary behavior of the velocity in the y-direction shows a great alignment, as depicted in Fig. 12(b). The PINN predicts $g(0) = 0$ and $g'(0) = 1$ with errors below 2×10^{-3} and under 2%, respectively, maintaining the physical no-slip and transverse flow conditions at the reference surface. The smooth monotonic decrease of $g(\eta)$ toward the far field and match with prescribed asymptotic values highlight the model's robustness in representing cross-flow momentum transport without spurious boundary constraints. The temperature $\theta(\eta)$, species concentration $\varphi(\eta)$, and microorganism density $\xi(\eta)$ exhibit similarly tight boundary condition observance from Fig. 12(c). Wall values are predicted within 10^{-4} relative error of the imposed conditions, confirming the PINN's accurate representation of thermal and mass flux boundary layers. Both temperature and concentration decrease smoothly to their far-field targets, consistent with theoretical decay expectations. The microorganism field also shows strong validation at the interface, ensuring the movement in the bioconvective nanofluid system. Far-field validation plots in Fig. 12(d) demonstrate that the expected asymptotic velocity and scalar field behaviors have been recovered by the PINN; as $\eta \to \infty$, the velocity gradient and field values are as close to their theoretical limiting values as possible; correspondingly, MAEs remain small $(< 10^{-3})$. Additionally, sustained consistency of PINN physics over the entire domain further provides confidence in the degree of implementation of PINN boundary conditions, which supports the overall accuracy of the PINN solutions and their physical realism at the global level of PINN solutions.

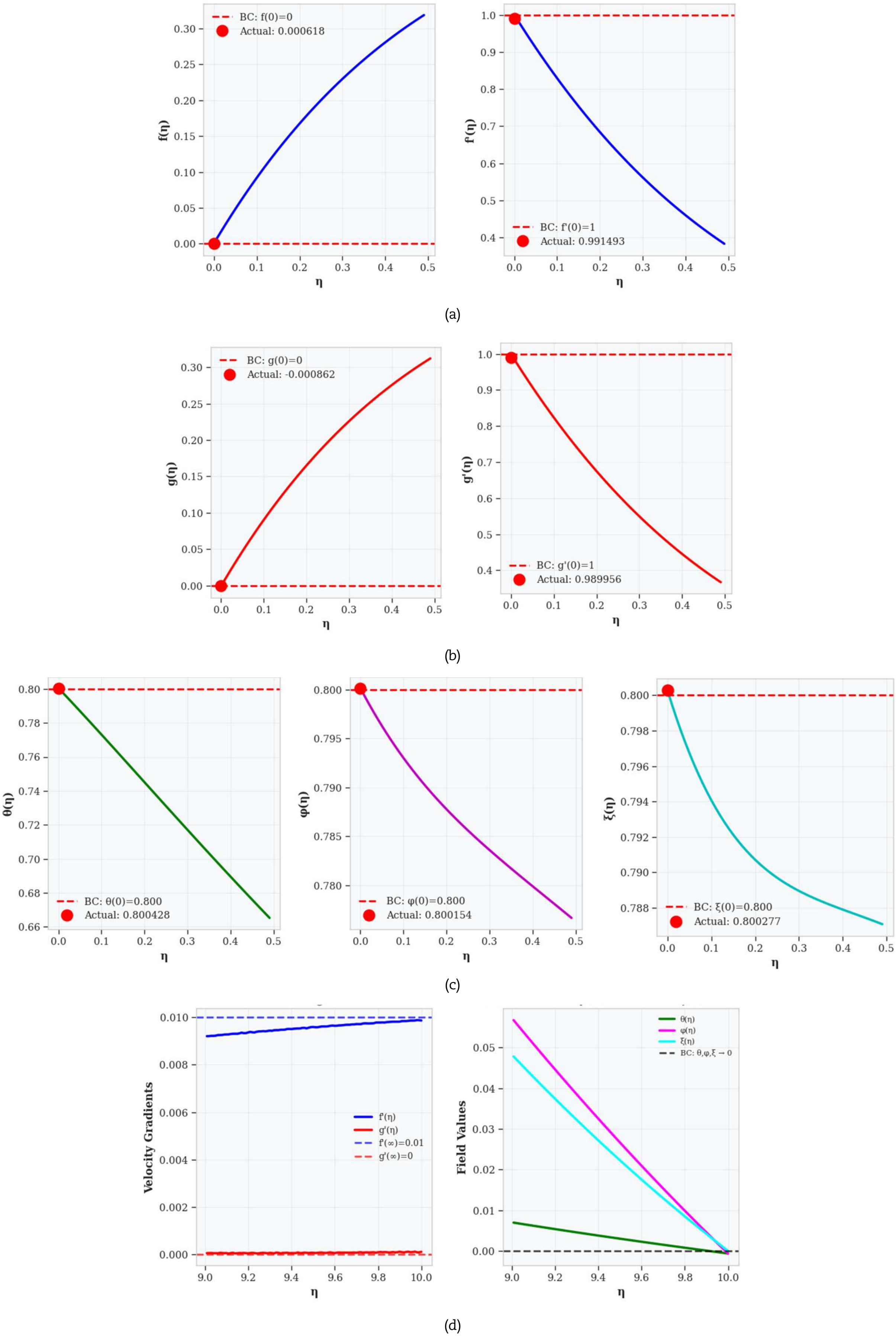

Fig. 12. (a) Velocity (x direction) boundary condition analysis, (b) Velocity (y direction) boundary condition analysis, (c) Temperature, species and microbial concentration boundary condition analysis, (d) Far-field boundary condition analysis.

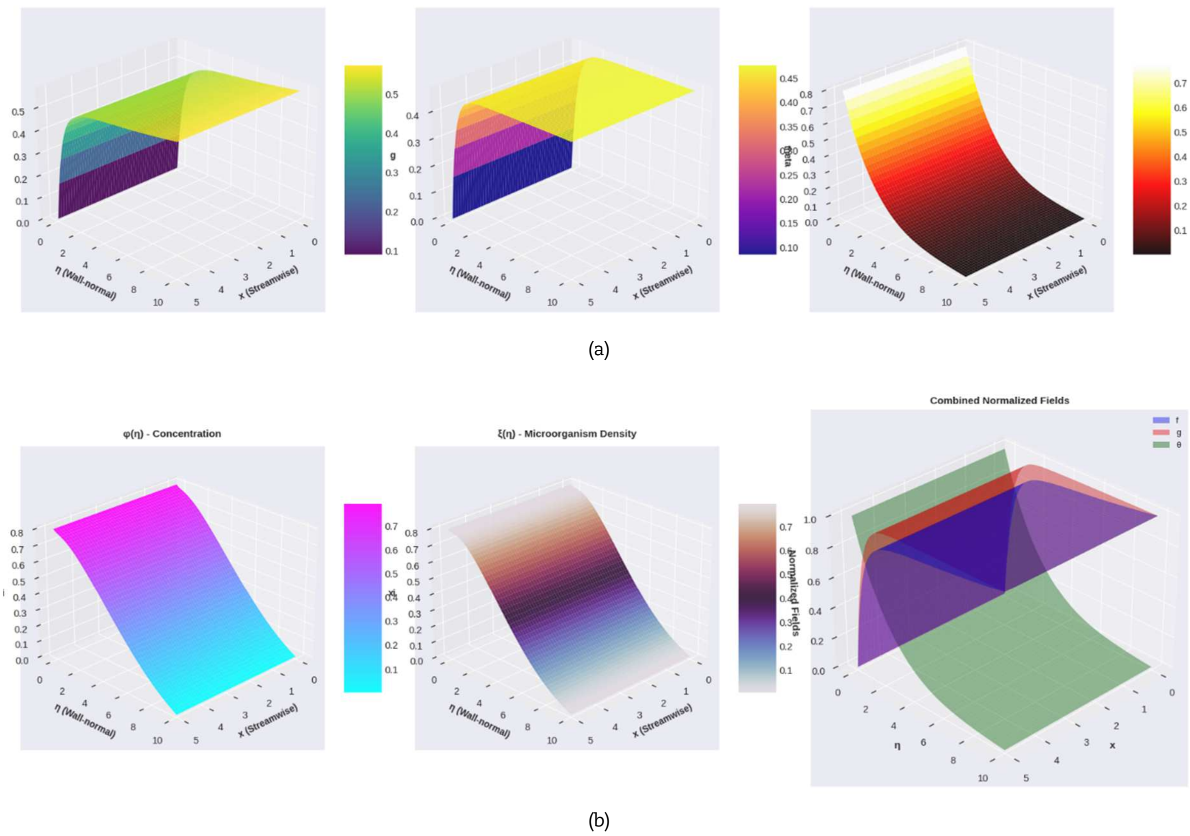

Fig. 13. (a) Surface plot for the velocity and temperature profiles, (b) Surface plot for the solutal and microbial density profiles.

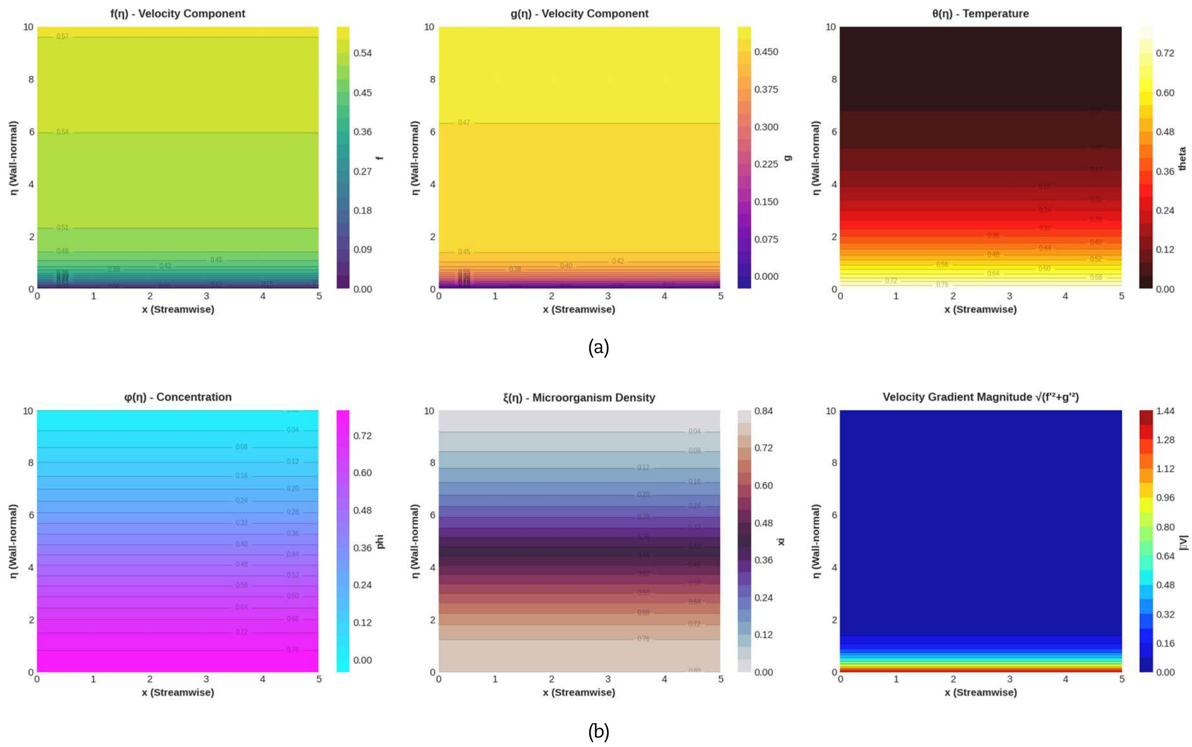

Fig. 14. (a) Contour plots for velocity and temperature profiles, (b) Contour plots for species and microbial concentration profiles.

The 3-D Surface plots depicting certain profiles are given in Fig. 13. The plots contained in Fig. 13(a) provide the primary solution fields of the Carreau-Yasuda bioconvective nanofluid model using the PINN solution methodology. The velocity components of the bioconvective nanofluid model represented by $(f(\eta))$ in the x-direction and $(g(\eta))$ in the y-direction, show smooth, physical boundary layer properties due to being generated from velocity conditions in the boundary regions that increase from no-slip wall to free-stream conditions of the nanofluid traveling along the model domain. Both the velocity profiles confirm the ability of the model in capturing shear-thinning and shear-thickening flow characteristics driven by the Carreau-Yasuda rheology.

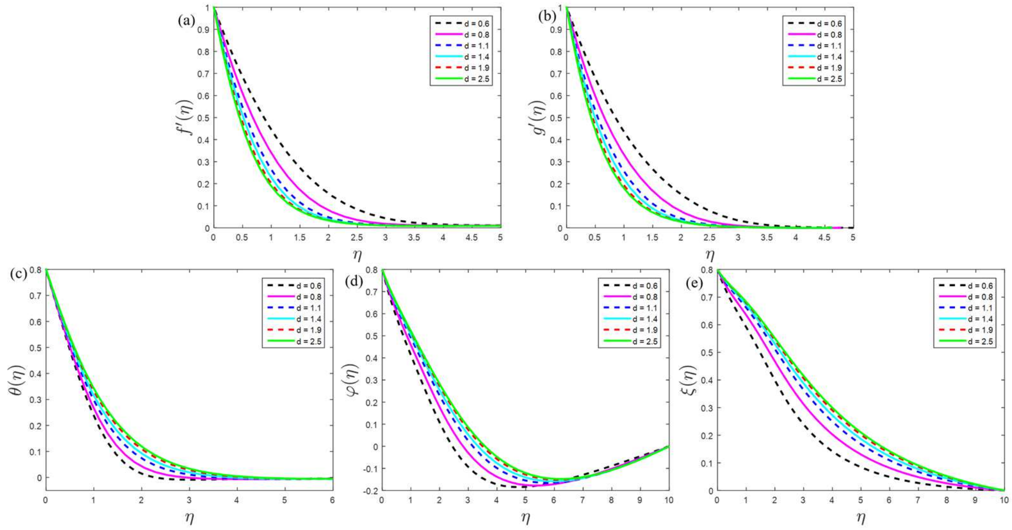

Fig. 15. Effect of the Carreau–Yasuda transition parameter d on fixed $n = 1.8$.

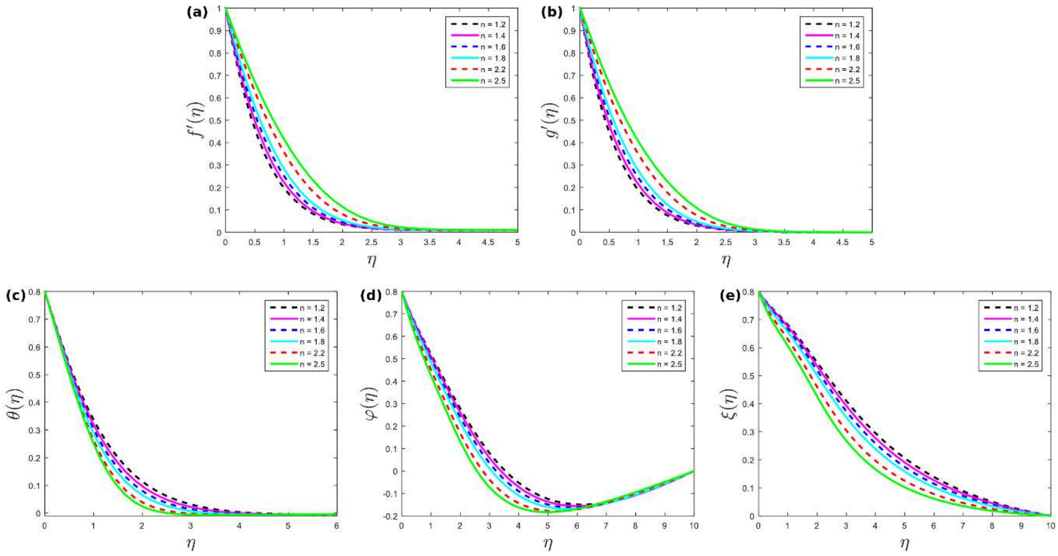

Fig. 16. Effect of the power-law index n on fixed $d = 1$.

The temperature field plot shows a shear gradient near the wall with monotonic decay moving into the domain, accurately reflecting thermal boundary layer formation according to established dimensionless numbers such as the Prandtl number. Fig. 13(b) presents the concentration and microbial concentration profiles. Both distributions exhibit boundary-layer profiles with steady decline into bulk regions. These results confirm the transport of solutal species and active microorganisms as governed by the coupled convection-diffusion-reaction equations. The inclusion of microorganism density highlights the bioconvective nature of the problem and the PINN's ability to capture this biophysical coupling accurately.

The contour plots in Fig. 14 reflect the characteristics of all profiles. Fig. 14(a) presents the velocity components in the x and y directions and the temperature distribution within the domain, revealing a clear boundary layer expansion and transport characteristics of the 3-dimensional bioconvective Carreau-Yasuda nanofluid flow modelled by the PINN. The streamwise velocity component $f(\eta)$ shows a concentrated velocity gradient near the wall, with flow accelerating sharply from zero at the no-slip boundary to its free-stream value, confirming proper shear-layer resolution, while the y-direction velocity component $g(\eta)$ exhibits a similar pattern with more gradual variation, capturing transverse flow phenomena essential for bioconvective transport. The thermal boundary layer is apparent as a steep temperature contour next to the wall and decreases to the temperature of the fluid bulk, which is typical of what would happen when thermal diffusivity and non-dimensional parameters for heat transfer are considered. These plots provide evidence showing that the PINN can usefully resolve both the momentum and thermal fields across coupled systems, with non-Newtonian flow types present.

The concentration and microorganism density contour maps, along with the velocity gradient magnitude, are represented in Fig. 14(b). The concentration profile shows a well-defined boundary layer with monotonically decreasing concentration values as the distance from the wall increases, and represents the effects of mass transport phenomena (i.e., convection and diffusion) described by the bioconvective Carreau-Yasuda flow model. The microorganism density contour (i.e., spatial distribution of microorganisms) shows the same general patterns (e.g., decay profiles) as those of the species transport system, which are consistent with bioconvection phenomena. Furthermore, the velocity gradient magnitude plot provides a representation of regions of high shear flow gradients (i.e., near the wall, within the boundary layer), which gives one an idea of local shear stress and level of mixing intensity in the system.

Figures 15 and 16 study the independent sensitivity of the solution profiles to the two Carreau-Yasuda parameters, d and power-law index n, by varying one while keeping the other constant ($n = 1.8$ in the d sweep, $d = 1$ in the n sweep).

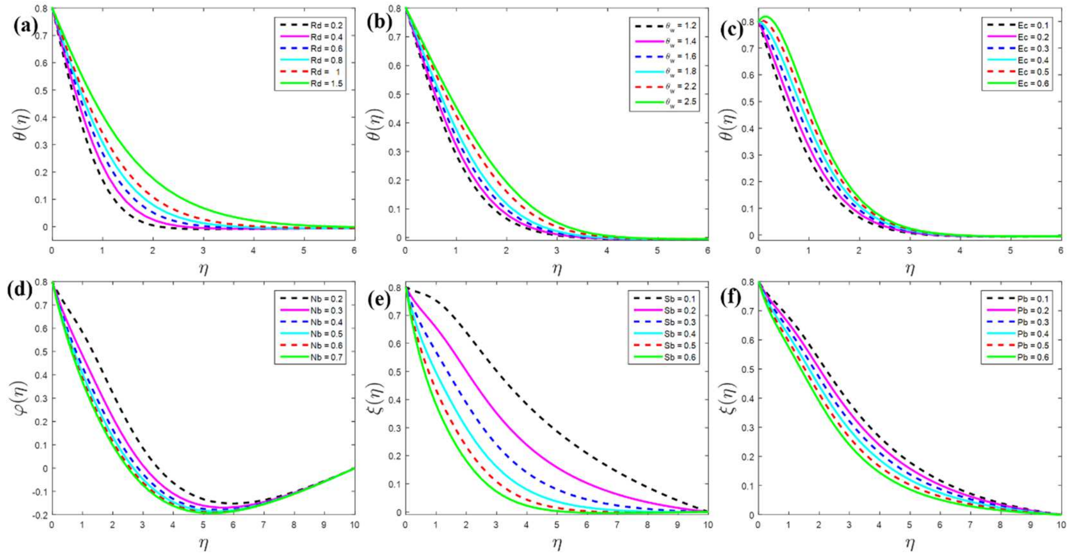

Fig. 17. Effect of the key parameters on the thermal, solutal, and microbial profiles.

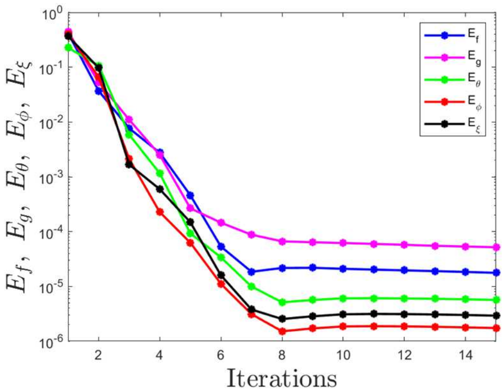

Fig. 18. Error graph of SQLM.

Since all the values of n considered in the sweeps $(1.2 \le n \le 2.5)$ and the constant value of n $(n = 1.8)$ in the d sweep are greater than unity, both sweeps are in the shear-thickening region for the entire range of variations. In this region, the two parameters have an opposing effect on the momentum profile: an increase in d causes a decrease in the momentum boundary layer (f', g' decay faster, Figs. 15(a,b)), while an increase in n causes an increase in the momentum boundary layer (f', g' decay slower, Figs. 16(a,b)).

The behavior of the thermal, solutal, and microbial layers is always opposite in both cases, becoming thicker for increasing d (Figs. 15(c-e)) but thinner for increasing n (Figs. 16(c-e)). Such a contrasting trend is understandable from their differing physical significance, the parameter n is responsible for the strength of effective viscosity growth with shear rate beyond the zero-shear regime, serving as an increased momentum diffusivity that widens the momentum layer when power-law index n increases whereas the Carreau-Yasuda parameter d determines the sharpness of this transition into the shear-thickening behavior, making the transition more abrupt and bringing it closer to the wall, narrowing the momentum layer and raising the scalar layers into the bulk of the domain as d increases. The influence of d saturates rapidly for $d > 1.1$, with the $d = 1.4, 1.7$, and 2.1 lines almost overlapping, whereas the influence of n slows a similar trend in the reverse, steepening rapidly for $n < 2$, where lines almost overlap but separate for higher values of the power-law index parameter.

Figures 17(a)-(c) show the effect of thermal radiation, temperature ratio parameter, and Eckert number on the temperature profile of the bioconvective Carreau-Yasuda nanofluid. As is clear from Figs. 17(a) and (b), an increase in both Rd and θ_w leads to a sharp rise in the fluid temperature and enlargement of the thermal boundary layer. In light of the quadratic thermal radiation of the Rosseland approximation, the heat flux caused by radiation is very nonlinear and strongly dependent on the temperature gradient. With an increase in these parameters, the nonlinearity of quadratic radiative heat transfer rises considerably, leading to a massive amount of thermal radiation being emitted to the non-Newtonian fluid system. In addition, it is evident from Fig. 17(c) that an increment in the Eckert number increases the thermal field. This is due to the process of viscous dissipation, whereby the shear rate of the Carreau-Yasuda fluid interacts with its internal resistance, causing a transformation of the kinetic energy into thermal energy. The graphs in Figs. 17(d)-(f) illustrate the distribution graphs of the nanoparticle concentration distribution function and motile microorganism density. Figure 17(d) illustrates that there is an increase in nanoparticle concentration within the boundary layer with an increase in the Brownian motion parameter. Increased Brownian forces cause enhanced randomness and chaotic collisions of nanoparticles in the Carreau-Yasuda fluid base. As a result, this enhances mass transfer and increases nanoparticle concentration distribution. However, Figs. 17(e) and 17(f) shows significant decrease in motile microorganism density with an increase in bioconvection the Schmidt number and bioconvection Peclet number. The increase in Sb causes low diffusivity of microorganisms compared to the momentum diffusivity of the non-Newtonian fluid and thus decreases the microorganism boundary layer thickness. At the same time, increased Pb causes the swimming velocity of the gyrotactic microorganism to exceed the random diffusion coefficient causing, rapid removal of the cells from the surface and decreasing the microbial distribution profile.

Table 3. Comparison of $-\theta'(0)$ and $-\varphi'(0)$ with [35] ($Pr = Le = 10, We_1 = We_2 = 0$).

Nb	Nt	$-\theta'(0)$			$-\varphi'(0)$		
		Ref. [35]	Present	Rel. Error (%)	Ref. [35]	Present	Rel. Error (%)
0.1	0.1	0.9524	0.95237	0.003	2.1294	2.12916	0.011
0.2	0.1	0.6932	0.69311	0.013	2.2740	2.27384	0.007
0.3	0.1	0.5201	0.52004	0.012	2.5286	2.52857	0.001
0.1	0.2	0.5056	0.50545	0.030	2.3819	2.38175	0.006
0.2	0.2	0.3654	0.36527	0.036	2.5152	2.51514	0.002
0.3	0.2	0.2731	0.27266	0.161	2.6555	2.65538	0.005
0.1	0.3	0.2522	0.25218	0.008	2.4100	2.40935	0.027
0.2	0.3	0.1816	0.18144	0.088	2.5150	2.51431	0.027
0.3	0.3	0.1355	0.13542	0.059	2.6088	2.60864	0.006

Table 4. Comparison of engineering quantities.

Quantity	PINN	SQLM	Abs Diff	Rel. Diff (%)
$C_{fx}\sqrt{Re_x}$	-2.51446900	-2.51648058	2.01e-03	-0.0799
$C_{fy}\sqrt{Re_y}$	-2.57277230	-2.57148591	1.29e-03	+0.0500
Nu_x/Re_x	0.53150445	0.53214226	6.38e-04	-0.1199
Sh_x/Re_x	0.08431652	0.08424907	6.75e-05	+0.0801
Nn_x/Re_x	0.08178261	0.08182350	4.09e-05	-0.0500

5. Comparison with Numerical Method

Numerical Method (SQLM): The Spectral Quasi-linearization method is the most effective technique for getting high accuracy while solving ordinary differential equations (ODEs) on a simple domain [9, 10]. The quasi-linearization method (SQLM) is a technique that uses the ideas of the Newton-Raphson method to linearize non-linear ordinary and partial differential equations. Like Newton's method, the QLM is derived from a one-term Taylor series about a previous approximation of the solution.

To validate the accuracy of the PINN approach, we compare our results with the SQLM, a well-established technique known for its spectral accuracy and faster convergence in solving nonlinear boundary layer problems [9, 10]. SQLM employs Chebyshev spectral collocation with quasi-linearization for the coupled nonlinear ODEs.

The convergence error graph for all the profiles of the considered model is shown in Fig. 18. It reflects the stability of the numerical method. The error for the velocity profiles, thermal, solutal, and microbial concentrations, with the number of iterations. The error reduced rapidly to 10^{-3} in the first few iterations (within 7-8 iterations) indicating the exponential convergence, while after that the slower rate of decrease represents the stabilization of the convergence to a minimum value. The error of all profiles are within the range of 10^{-3} to 10^{-6} is quite small and indicates the robustness and balanced solution across all parameters, that converses to a higher rate of accuracy of the solution.

The comparison between the SQLM and PINN reveals remarkable consistency and accuracy in the simulation of 3D bioconvective Carreau-Yasuda nanofluid flow. The SQLM error graph demonstrates robust convergence, with errors stabilizing between 10^{-3} and 10^{-6}, indicating that SQLM provides an accurate solution with minimal residual errors across the computational domain. While PINN achieves similar levels of accuracy, validated by the low mean absolute errors, residual histograms, and other results described throughout the results and plots.

For the validation of the SQLM solution method without taking into account the current bioconvective phenomenon, we consider a comparison of it with the classical nanofluid stretching-sheet problem by Khan and Pop [35], which is derived as a particular case from the current analysis ($We_1 = We_2 = 0, M = Rd = Rb = \lambda = Ec = \delta_T = \delta_C = 0, S_1 = S_1 = S_1 = 0, Pr = 10, Le = 10$). Table 3 gives the values of the local Nusselt and Sherwood numbers, $-\theta'(0)$ and $-\varphi'(0)$, for nine different cases of the parameters of Brownian motion Nb and thermophoresis Nt, demonstrating excellent agreement with the results reported in [35] with a maximum error of 0.16%.

The comparison of the engineering quantities predicted from the PINNs with the spectral quasi-linearization method is given in Table 4. These engineering quantities, such as drag function in the x and y-directions, the heat transfer (local Nusselt number), and mass transfer (Sherwood number) with the bio-mass transfer (Microbial density number) rates, are crucial for optimizing heat/mass transfer phenomena in engineering applications. It is worth clarifying that the SQLM convergence error and the PINN training loss are not directly comparable quantities. The former measures the change in the solution itself between successive quasi-linearization iterates, while the latter measures the mean-squared residual of the governing equations and boundary conditions evaluated at the training collocation points. A small training loss does not, by itself, establish a correspondingly small error in the PINN's predicted field values relative to the true solution. The relevant accuracy comparison is instead the direct pointwise agreement between the PINN and SQLM solution fields, reported below.

The PINN results are closely aligned with SQLM, validating the accuracy of the physics-informed neural network approach for this complex multi-physics problem. The identical values for the engineering quantities, including skin friction coefficients, local Nusselt numbers, species, and biomass transfer rates, for the PINNS and SQLM, with the relative differences below 0.12%, suggest the ability of PINNs as a feasible and flexible alternative to the traditional spectral methods. The other analysis, such as statistical analysis of field profiles, further highlighted that the PINN captures the detailed spatial structures of velocity, temperature, concentration, and microorganism concentration transfer rates. Beyond these engineering quantities in Table 4, we additionally compare the PINN and SQLM solutions pointwise across the domain. The maximum absolute differences are small for all five fields ($|\Delta f| \leq 1.64 \times 10^{-3}, |\Delta g| \leq 1.31 \times 10^{-3}, |\Delta\theta| \leq 9.85 \times 10^{-4}, |\Delta\varphi| \leq 9.85 \times 10^{-4}, |\Delta\xi| \leq 6.57 \times 10^{-4}$), and mean relative differences remain below 0.6% for f, g, φ, and ξ. The mean relative difference for θ is higher (5.4%), and the maximum relative differences reported for θ and φ (up to several hundred percent at isolated points) are artifacts of these two fields passing through zero within the domain (Fig. 3(b)), where relative-percentage error is not a meaningful metric regardless of absolute accuracy; the absolute differences at these points remain of the same small magnitude as elsewhere. Averaged across all five fields, the mean relative error is 1.26%, indicating close but not exact pointwise agreement between the two solution methods for this parameter set.

Table 5. Computational comparison of methods.

Method	Computational task	CPU time (s)	CPU time (min)
SQLM	Iterative solution + generation of five profiles	8.74	0.146
PINN	20,000 training epochs	1660.6	27.68

Overall, this close alignment of comparison validates the use of PINNs as a reliable, mesh-free alternative to the spectral methods for solving high-dimensional, complex fluid flow problems. These findings suggest that PINNs provide a consistent mesh-free alternative for steady boundary-layer problems, while SQLM retains advantages in deterministic spectral accuracy and computational efficiency.

While both methods yield comparable numerical accuracy, their computational characteristics differ. The SQLM approach demonstrates rapid convergence owing to its spectral discretization and quasi-linearization strategy, making it computationally efficient for steady deterministic boundary-layer systems. In contrast, the PINN framework requires iterative optimization over multiple training epochs, resulting in higher computational time. However, PINNs offer flexibility in handling parametric variations and can be extended to inverse or data-assimilation settings without reformulating the discretization procedure.

The computational cost of the PINN framework was approximately 1660 s (27.7 minutes) on a CPU platform for 20,000 training epochs with 3,000 collocation points. In contrast, spectral quasi-linearization methods in the context of the current parameter set needed just 8.74 seconds of wall time as shown in Table 5. Clearly, the PINN needed roughly 190 times the amount of wall-time. Such a contrast highlights the computational advantage of SQLM for solving the current forward BVP. SQLM is the ideal approach if computational efficiency and deterministic forward accuracy are the main concerns; on the other hand, if a mesh-free approach is desirable along with possible future developments toward inverse, parametric, or data-driven problems, then PINN will be flexible.

6. Conclusion

The Physics-Informed Neural Network (PINN) model was applied for the three-dimensional, triple-stratified, bioconvective Carreau-Yasuda nanofluid boundary layer flow under the effects of magnetic field, dual-variable conductivity, and quadratic thermal radiation, using a reference solution obtained by the Chebyshev spectral quasi-linearization method (SQLM). With regards to the triple stratification and bioconvection as mentioned in the objectives of this study, the results can be summed up as follows:

- The PINN framework successfully computes the solution of the coupled field velocities (from fluid flow), temperatures (from heat transfer), concentrations (of solutes), and microbial densities (from biological activities), which are calculated in an implementation consistent with both the enforcing physical laws governing velocity, temperature, concentration, and density as well as the specified boundary conditions.
- It confirms the robustness of the model and its basis in the governing equations; the residuals associated with the governing equations of momentum, energy, concentration of solute, and concentration of bacteria, as well as checking conformance to the boundary conditions, validate the computationally consistent application of the PINN approach within the full range of parameters considered.
- The trained PINN fulfils all the boundary conditions with maximum absolute errors less than 2.7×10^{-4}, indicating that the training process satisfies the boundary condition constraints, while about 96% of the collocation points satisfy the governing equation constraints with residual errors less than 10^{-2}.
- The predicted engineering-critical outputs (skin friction coefficients and rates of heat and mass transfer) have been found to agree with the SQLM reference within 0.12% for all five quantities considered and within 0.6% for most field variables, thus proving the ability of the PINN to accurately reproduce the reference solution of the SQLM.
- The comparison of the SQLM outputs to the comparable outputs from the PINN approach shows the close agreement in output rates and variabilities, confirming that the PINN will serve as a viable alternative mesh-less method for predicting the behaviour of natural boundary layer flows at a steady state.
- Surface and parametric plots show that the PINN framework can describe the spacewise behavior of velocity and temperature fields under various physical parameters, including the triple stratification structure and the microorganisms layer thickness, which was higher than the thermal and solutal boundary layer thickness due to the bioconvection Peclet and Lewis numbers' effects.
- The performance from the computational perspective, the SQLM is more quickly computable when determining the steady-state behaviour of problems with known inputs/outputs, as compared to the PINN approach, which has the potential for varying parameter inputs and could be used to develop data-driven modelling solutions.

From the perspective of engineering application, the current coupled system of radiative, bioconvective, and nanofluid flow problems can be regarded as a typical example of solar-powered microbial bioreactor or biofuel cell configurations where layered flow, magnetically driven fluid motion, and shear-dependent rheology of microorganism-incorporated fluid can co-exist under varying heat loading. The current PINN trained using fixed parameters, is able to offer a mesh-free solution in comparison to SQLM for solving such steady-state problem classes where all input and output information is readily available; and for future applications which include but are not limited to parametric PINNs based on the full governing parameter vector, solving inverse problems; and incorporating experimental data.

Author Contributions

S. Mishra was solely responsible for conceptualization, mathematical modeling, software development, data generation, formal analysis, and manuscript preparation. The author discussed the results, reviewed, and approved the final version of the manuscript.

Acknowledgments

Not Applicable.

Conflict of Interest

The author declared no potential conflicts of interest concerning the research, authorship, and publication of this article.

Funding

The author received no financial support for the research, authorship, and publication of this article.

Data Availability Statements

The datasets generated and/or analyzed during the current study are available from the corresponding author on reasonable request.

Nomenclature

a	Stretching rate constant
b	Free-stream velocity constant
A	Velocity ratio parameter, b/a
B_0	Applied magnetic field strength
C	Nanoparticle concentration
c_p	Specific heat capacity
Cr	Chemical reaction rate parameter
d	Carreau–Yasuda rheological index
D_B	Brownian motion parameter
D_T	Thermophoresis parameter
D_N	Microbial thermophoresis diffusion
Ec	Eckert number
f	Dimensionless streamwise velocity functions
g	Dimensionless transverse velocity functions
g_t	Gravitational acceleration
k_∞	Thermal conductivity at ambient
k^*	Mean absorption coefficient
Lb_1, Lb_2	Non-dimensional coefficients of the mixed streamwise cross-diffusion terms in the Cattaneo–Christov relaxation
C_{fx}, C_{fy}	Skin friction coefficients (x, y)
Nu_x, Sh_x	Local Nusselt and Sherwood number
Re_x, Re_y	Local Reynolds numbers
α	Thermal diffusivity
β	Volumetric thermal expansion coefficient
Γ	Carreau–Yasuda material rate constant
δ	Shear-rate regularization parameter
δ_T, δ_C	Thermal and solutal relaxation (Cattaneo–Christov) parameters
ν	Kinematic viscosity
ρ_f, ρ_m	Density of fluid and microorganism
ρ_p	Density of nanoparticle
ω_1, ω_2	Thermal and solutal conductivity coefficients
Le	Lewis number
M	Hartmann (magnetic) number
m	Chemotaxis constant
n	Power-law parameter
N	Motile microorganism density
Nb	Brownian motion parameter
Np	Bioconvection Brownian motion
Nt	Thermophoresis parameter
Nr	Buoyancy ratio parameter
Pb	Bioconvection Péclet number
Pr	Prandtl number
q_m	Mass flux at wall
q_n	Microbial flux at wall
q_w	Bioconvection Rayleigh number
Rd	Heat flux at wall
Rb	Thermal radiation parameter
Sb	Bioconvection Schmidt number
S_1, S_2, S_3	Thermal, solutal, microbial stratification parameters
T	Fluid temperature
u, v, w	Velocity components (x, y, z)
We_1, We_2	Local Weissenberg numbers (x, y)
Nn_x	Local microbial density number
η	Similarity variable
θ	Dimensionless temperature parameter
θ_w	Temperature ratio parameter
Λ_T, Λ_C	Thermal and solutal flux relaxation times
μ_0, μ_∞	Zero-shear-rate, infinite-shear-rate viscosity
ξ	Dimensionless microorganism density
σ , σ^*	Electrical conductivity, Stefan–Boltzmann
τ	constant
φ	Nanoparticle-to-base-fluid heat capacity ratio dimensionless concentration
Ω	Constant microorganism concentration-difference parameter

References

[1] Raissi, M., Perdikaris, P., Karniadakis, G.E., Physics-informed neural networks: A deep learning framework for solving forward and inverse problems involving nonlinear partial differential equations, *Journal of Computational Physics*, 378, 2019, 686-707.

[2] Zhang, J., Liu, H., Chen, W., A comprehensive review of advances in physics-informed neural networks for complex fluid dynamics, *Physics of Fluids*, 36, 2024, 101301.

[3] Smith, E., Wang, L., Hernandez, M., Physics-informed neural networks for fluid flow analysis: Re-initialization strategy for stiff problems, *Scientific Reports*, 15, 2025, 13127.

[4] Patel, R., Nguyen, T., Exploring data-free physics-informed neural network solvers for fluid mechanics applications, *arXiv preprint arXiv:2411.15410*, 2024, 1-15.

[5] Reyes, B., Zhao, F., Li, D., et al., Learning unknown physics of non-Newtonian fluids via physics-informed neural networks, *Physical Review Fluids*, 6, 2021, 073301.

[6] Arif, M.S., Abodayeh, K., Nawaz, Y., An application of the finite element method for heat and mass transfer of boundary layer flow using variable thermal conductivity and mass diffusivity, *Journal of Mathematics*, 2022, 2022, 1-14.

[7] Mishra, S.C., Muthukumaran, R., Maruyama, S., The finite volume method approach to the collapsed dimension method in analyzing steady/transient radiative transfer problems in participating media, *International Communications in Heat and Mass Transfer*, 38, 2011, 291-299.

[8] Mishra, S., Mondal, H., Behl, R., Salimi, M., The impact of thermal radiation on mixed convective unsteady nanofluid flow in a revolving vertical cone, *Mathematics*, 12, 2024, 349.

[9] Mishra, S., Mondal, H., Kundu, P.K., Dynamics of magneto-bioconvection thermal casson nanofluid with activation energy and joule heating, *Numerical Heat Transfer, Part B: Fundamentals*, 86, 2025, 3854-3870.

[10] Mishra, S., Mondal, H., Rotational microorganism magneto-hydrodynamic nanofluid flow with Lorentz and Coriolis force on moving vertical plate, *BioNanoScience*, 14, 2024, 955-968.

[11] Mishra, S., Mondal, H., Kundu, P.K., Entropy optimisation of a viscous bioconvective nanofluid flow with Coriolis and Lorentz forces using bivariate spectral quasi-linearisation technique, *Pramana - Journal of Physics*, 99, 2025, 1-12.

[12] Jebali, M., Rehman, S., Asiri, F., et al., AI-driven modeling and simulation for entropy optimized radiative Darcy-Forchheimer flow of micropolar tri-hybrid nanofluid at a stagnation point, *Propulsion and Power Research*, 15, 2026, 48–66.

[13] Ali, H., Shah, M., Khan, R., Artificial neural network (ANN) analysis on thermophysical properties of nanofluids for heat transfer applications, *PLoS One*, 19, 2024, e0281357.

[14] Sahu, K.K., Verma, M., Singh, A., Levenberg-Marquardt recurrent neural network for heat transfer analysis of ternary hybrid nanofluids over a spinning disk, *Journal of Thermal Analysis and Calorimetry*, 150, 2025, 1-15.

[15] Mishra, S., Mondal, H., A neuro-computational proposal for the ZrO2-Fe3O4 nanoparticles in the engine oil–based hybrid nanofluid, *BioNanoScience*, 14, 2024, 4985-4998.
[16] Rehman, S., Farooq, A., Coupling physics-informed neural networks and regression techniques for modeling cubic stratified nanofluid flow in magnetic fields, *Chinese Journal of Physics*, 102, 2026, 29-47.
[17] Rehman, S., Farooq, A., Iqbal, M.A., Neuro-heuristic and regression-based modeling of three-dimensional Williamson–micropolar nanofluid flow with regularization and uncertainty quantification, *Engineering Applications of Artificial Intelligence*, 166, 2026, 113667.
[18] Zhao, Z., Wang, Y., Zhang, W., Ba, Z., Physics-informed neural networks in heat transfer-dominated multiphysics systems: A comprehensive review, *Engineering Applications of Artificial Intelligence*, 157, 2025, 111098.
[19] Kananipour, M., Mohseni, M.M., Jahanmardi, R., Khonakdar, A.A., Heat and mass transfer analysis of s-PTT nanofluid in microchannels under combined electroosmotic and pressure-driven flows with wall slip using the homotopy perturbation method, *Heliyon*, 10, 2024, e39526.
[20] Qayyum, M., Jan, A., Khan, A., Analysis of blood flow of unsteady Carreau-Yasuda fluid with chemical reaction, Brownian motion and thermophoresis effects, *Computers in Biology and Medicine*, 103, 2023, 107844.
[21] Waqas, H., Khan, S.U., Bhatti, M.M., Imran, M., Significance of bioconvection in chemical reactive flow of magnetized Carreau–Yasuda nanofluid with thermal radiation and second-order slip, *Journal of Thermal Analysis and Calorimetry*, 140, 2020, 1293-1304.
[22] Chen, T., Chu, B., Shi, M., Heat transfer analysis of Carreau-Yasuda nanofluid flow with quadratic thermal radiation, *Journal of Computational Design and Engineering*, 11, 2023, 99–115.
[23] Akbar, Y., Chen, C., et al., Intelligent modeling of thermal transport in peristaltic flow of nanofluid through porous media using response surface and neural networks, *International Communications in Heat and Mass Transfer*, 174, 2026, 110901.
[24] Salam, A., Shah, S., Ali, N., Neural and neuro-fuzzy simulation of mixed convective magneto-Carreau nanofluid over an inclined plate, *Results in Engineering*, 19, 2025, 102246.
[25] Raafat, P.B., Ibrahim, F.N., Sharaf, M.A.M., Characterizing thermal efficiency and entropy generation of Sisko nanofluids in parabolic trough solar collectors: A comparison between three carbon-based nanoparticles, *Experimental and Computational Multiphase Flow*, 7, 2025, 551–565.
[26] Kumar, D., Singh, P., Dynamics of bioconvection-driven fluid flow through Riga plates in the presence of triple stratifications, *Journal of Molecular Liquids*, 394, 2025, 123476.
[27] Oreyeni, T.S., Ismail, S.O., Pop, I., Exploring the impact of stratification on the dynamics of bioconvective nanofluid flow: A triple stratified approach, *Results in Physics*, 54, 2024, 106543.
[28] Mishra, S., Mondal, H., Kundu, P.K., Impact of microbial activity and stratification phenomena on generating/absorbing Sutterby nanofluid over a Darcy porous medium, *Journal of Applied and Computational Mechanics*, 9, 2023, 1112-1125.
[29] Bhatti, M., Khan, N., Nanofluid bioconvection in water-based suspensions containing nanoparticles and oxytactic microorganisms, PLoS One, 6, 2011, e16327.
[30] Khan, D., Iqbal, M., Bioconvection micropolar nanofluid through stretching surface, *ACS Omega*, 7, 2022, 10145–10157.
[31] Mishra, S., Mondal, H., Kundu, P.K., Unsteady bioconvection microbial nanofluid flow in a revolving vertical cone with chemical reaction, *Pramana - Journal of Physics*, 98, 2024, 12.
[32] Ali, A., Khan, Z., Neural network analysis of bioconvection effects on heat and mass transfer in non-Newtonian chemically reactive nanofluids, *Case Studies in Thermal Engineering*, 45, 2024, 102156.
[33] Waqas, H., Farooq, U., Khan, S.A., Numerical analysis of dual variable of conductivity in bioconvection flow of Carreau–Yasuda nanofluid containing gyrotactic motile microorganisms over a porous medium, *Journal of Thermal Analysis and Calorimetry*, 145, 2021, 2033-2044.
[34] Waqas, H., Imran, M., et al., Cattaneo–Christov double diffusion and bioconvection in magnetohydrodynamic three-dimensional nanomaterials of non-Newtonian fluid containing microorganisms with variable thermal conductivity and thermal diffusivity, *Waves in Random and Complex Media*, 35, 2025, 5759-5778.
[35] Kumar, S., Desai, R., Thermal analysis and generalized Cattaneo-Christov concept in stagnation point Maxwell nanofluid flow, *International Journal of Engineering Research and Technology*, 13, 2024, 44–57.
[36] Chen, Y., Xu, L., Heat transfer analysis of Maxwell hybrid nanofluid with variable thermal conductivity, *Alexandria Engineering Journal*, 82, 2023, 1347–1359.
[37] Sharma, R., Kumar, V., Nonlinear Boussinesq and Rosseland approximations on 3D magnetohydrodynamic Carreau nanofluid flow, *AIMS Mathematics*, 9, 2022, 1549–1568.
[38] Mishra, S., Mondal, H., Dhlamini, M., Comparative analysis of the linear, non-linear, and quadratic thermal radiation on polar fluid flow, *International Journal of Computational Methods in Engineering Science and Mechanics*, 27, 2026, 129-146.
[39] Malik, M.Y., Shah, N., Flow of nanoliquid past a vertical plate with novel quadratic thermal radiation, *International Communications in Heat and Mass Transfer*, 113, 2020, 104492.
[40] Li, Y., Zhou, H., Zhang, Y., Physics-informed neural networks in heat transfer-dominated flows, *Engineering Applications of Artificial Intelligence*, 119, 2025, 111098.
[41] Rana, S., et al., Thermal enhancement in coolant using novel hybrid Carreau-Yasuda nanofluid and triple stratification, *Results in Engineering*, 5, 2021, 105417.
[42] Lee, T.Y., Chen, Z., Design and optimization of heat transfer channel using physics-informed neural networks (PINN) and deep Gaussian processes, *Energy Conversion and Management*, 286, 2025, 117692.
[43] Lee, J., et al., Physics informed neural networks for fluid flow analysis: Overcoming the challenges of stiff problems, *Scientific Reports*, 15, 2025, 1-15.
[44] Heger, P., et al., Investigation of physics-informed deep learning for the prediction of three-dimensional flow fields in aerothermal vehicle simulations, *Aerospace Science and Technology*, 146, 2024, 108920.
[45] Huang, A.J., et al., On the limitations of physics-informed deep learning, *arXiv preprint arXiv:2311.12345*, 2023, 1-12.
[46] Iqbal, J., Abbasi, F.M., Theoretical investigation of MHD peristalsis of non-newtonian nanofluid flow under the impacts of temperature-dependent thermal conductivity: Application to biomedical engineering, *ZAMM - Journal of Applied Mathematics and Mechanics*, 104, 2024, e202300724.
[47] Akbar, Y., Mao, X., et al., Thermodynamic analysis of nanofluid with aggregated and non-aggregated nanoparticles, *International Journal of Heat and Fluid Flow*, 118, 2026, 110205.
[48] Kayikci, S., Computational insights of bioconvective third grade nanofluid flow past a riga plate with triple stratification and swimming microorganisms, *Journal of Mathematics*, 2022, 2022, 6378721.
[49] Waqas, H., Imran, M., Bhatti, M.M., Bioconvection aspects in non-Newtonian three-dimensional Carreau nanofluid flow with Cattaneo–Christov model and activation energy, *The European Physical Journal Special Topics*, 230, 2021, 1317-1328.
[50] Oreyeni, T., Ramesh, K., Nayak, M.K., Oladele, P.A., Triple stratification impacts on an inclined hydromagnetic bioconvective flow of micropolar nanofluid with exponential space-based heat generation, *Waves in Random and Complex Media*, 32, 2022, 1-22.
[51] Algehyne, E.A., Alamrani, F.M., Saeed, A., Homotopy assessment on the stratified micropolar Carreau–Yasuda bio-inspired radiative copper and gold/blood nanofluid flow on a Riga plate, *Journal of Thermal Analysis and Calorimetry*, 150, 2025, 2347-2360.

ORCID iD

Shweta Mishra https://orcid.org/0000-0003-3590-2883

How to cite this article: Mishra S. Simulation of Triple Stratified 3-D Bioconvective Non-Newtonian Nanofluid Flow using Physics-Informed Neural Network, *J. Appl. Comput. Mech.*, xx(x), 2026, 1–24. https://doi.org/10.22055/jacm.2026.49407.5954